

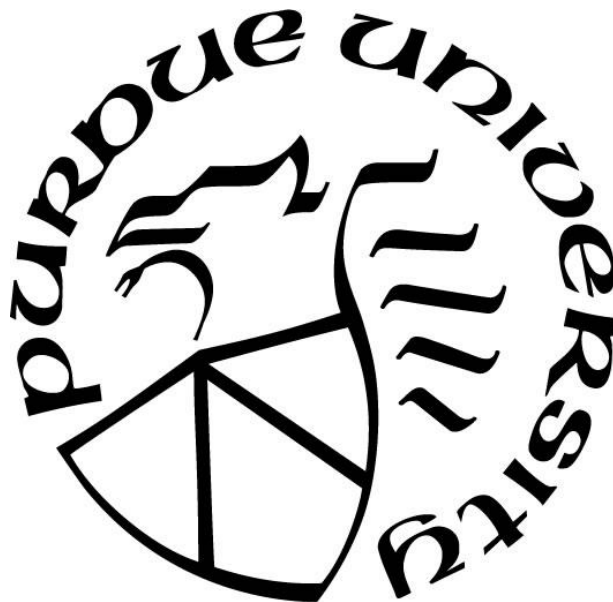
**ANALYSIS OF FRICTION STIR ADDITIVE MANUFACTURING AND
FRICTION STIR WELDING OF AL6061-T6 VIA NUMERICAL
MODELING AND EXPERIMENTS**

by
Nitin Rohatgi

A Thesis

*Submitted to the Faculty of Purdue University
In Partial Fulfillment of the Requirements for the degree of*

Master of Science in Mechanical Engineering



Department of Mechanical Engineering
West Lafayette, Indiana
December 2020

THE PURDUE UNIVERSITY GRADUATE SCHOOL
STATEMENT OF COMMITTEE APPROVAL

Dr. Yung C. Shin, Chair

Department of Mechanical Engineering

Dr. Martin Byung-Guk Jun

Department of Mechanical Engineering

Dr. Marcial Gonzalez

Department of Mechanical Engineering

Approved by:

Dr. Nicole L. Key

ACKNOWLEDGMENTS

Throughout my research, I have received a great deal of help and support from many people. I want to take this opportunity to express my appreciation and gratitude to everyone who supported me with this project.

I would like to express my sincere gratitude to my advisor, Dr. Yung Shin, for providing me his guidance and an opportunity to work on this exciting topic for my master's thesis. I am thankful for his constant support, valuable suggestions, and guidance throughout the course of my research.

I would also like to thank my thesis committee members, Dr. Martin Byung-Guk Jun and Dr. Marcial Gonzalez, for their valuable suggestions and insightful comments towards my thesis.

I would like to thank my fellow group members Mohamed Elkhateeb, Kyung-min Hong, Bin Zhang, Corbin Grohol, and others, for their time and cooperation and for helping me in this research. I am thankful to the staff at ME Machine shop and Bechtel Innovation Design Center for extending their facilities for my research. I would also like to extend my appreciation to Nikhil Sharma for his help with experiments.

Lastly, I would like to thank my parents and family for their constant support and encouragement. I am also thankful to my friends for keeping me in good spirits during my studies.

TABLE OF CONTENTS

LIST OF TABLES	6
LIST OF FIGURES	7
ABSTRACT	10
1. INTRODUCTION	11
1.1 Motivation.....	11
1.2 Background	12
1.2.1 Friction stir welding.....	12
1.2.2 Defects in friction stir welding.....	15
1.2.3 Shortcomings of fusion-based additive manufacturing	16
1.2.4 Friction stir additive manufacturing	17
1.3 Literature review	18
1.3.1 Numerical modeling of friction stir welding.....	18
1.3.2 Friction stir additive manufacturing	21
1.4 Thesis objectives	22
1.5 Thesis outline	23
2. EXPERIMENTAL SETUP	25
2.1 Friction stir welding setup	25
2.2 Friction stir additive manufacturing setup	26
2.3 Sample preparation and mechanical testing.....	29
3. FINITE ELEMENT MODEL.....	30
3.1 Friction stir welding.....	30
3.1.1 Model, Assembly, Mesh and Material Properties	30
3.1.2 Contact, Interactions and Boundary conditions	32
3.1.3 Model validation.....	34
3.2 Friction stir additive manufacturing	37
3.2.1 Model, Assembly, Mesh and Material Properties	37
3.2.2 Contact, Interactions and Boundary conditions	38
3.2.3 Model validation.....	39
4. RESULTS AND DISCUSSIONS.....	42

4.1	Friction stir welding.....	42
4.1.1	Sound weld.....	42
4.1.2	Defect formation in FSW.....	43
	Tunnel defect.....	43
	Cavity defect.....	45
4.2	Friction stir additive manufacturing	46
4.2.1	Peak temperatures observed in the model.....	46
4.2.2	Microstructure observation	49
4.2.3	Microhardness analysis.....	54
	Material behavior.....	54
	Observation and comparison	55
4.2.4	Analysis of mechanical properties.....	59
	Tensile test.....	59
	Tensile shear test.....	62
4.2.5	Defects observed	65
5.	CONCLUSIONS.....	69
5.1	Conclusions.....	69
5.2	Future work and applications	70
	REFERENCES	72

LIST OF TABLES

Table 3-1: Johnson Cook material parameters for Al6061.	32
Table 3-2: The experimental and simulated parameters of the welding cases.	34
Table 3-3: Comparison between the measured experimental axial forces and the simulated axial forces.	35
Table 4-1: Temperature ranges for different phases.	55
Table 4-2: Tensile shear test results with the calculated joint efficiency.....	65

LIST OF FIGURES

Figure 1-1: Welding schematic for Friction Stir Welding [8].	14
Figure 1-2: Effect of process parameters on weld defects [25].	16
Figure 1-3: Schematic of Friction stir additive manufacturing [56].	22
Figure 2-1: Friction stir welding tool.	25
Figure 2-2: Friction stir welding setup.	26
Figure 2-3: Experimental Setup for Friction stir additive manufacturing.	27
Figure 2-4: The top view of the weld adding 5 plates on the substrate.	28
Figure 2-5: The FSAM part.	28
Figure 2-6: The cross-section of the FSAM processed area.	29
Figure 3-1: The featured tool used in the simulations.	31
Figure 3-2: Assembly and mesh used in the FE model.	31
Figure 3-3: Boundary conditions employed in FSW simulations.	34
Figure 3-4: Plot comparing of experimental axial force and simulated axial force.	36
Figure 3-5: Experimental stir zone (a); Simulated stir zone (b).	36
Figure 3-6: Assembly of the FE model.	37
Figure 3-7: Boundary conditions for FSAM simulations.	38
Figure 3-8: Comparison of Axial Forces between Experiment and FE model.	40
Figure 3-9: Comparison between the experimental stir zone and the simulated stir zone.	41
Figure 4-1: Sound weld cross-section (at the center of the model). (Top left pointing blue arrow-shoulder-driven flow; down left pointing orange arrow- pin-driven flow).	42
Figure 4-2: Temperature distribution around the tool during sound weld formation.	43
Figure 4-3: Temperature distribution in the case of tunnel defect.	44
Figure 4-4: EVF_Void distribution in the case of Tunnel defect. A void is noticed at the advancing side.	44
Figure 4-5: Temperature distribution in the case of tunnel defect.	45
Figure 4-6: EVF_Void distribution in the case of Cavity defect. A void is noticed at the advancing side.	46
Figure 4-7: Temperature contour at the cross-section.	47

Figure 4-8: Peak temperature plot horizontally. Data points numbered correspond to the location on Figure 4-14.....	48
Figure 4-9: Peak temperature plot in the vertical direction. Data points numbered correspond to the location on Figure 4-14.....	49
Figure 4-10: Macrostructure after Weck's etching with the various zones and location for the images.....	50
Figure 4-11: Optical Micrographs of Base metal (Location 1), Heat Affected Zone (Location 2), Thermo-mechanically affected zone (Location 3), and Stir zone (Location 4).....	50
Figure 4-12: SEM Micrograph of the TMAZ around the tool at locations a, b and c; SEM Micrograph of the HAZ at location 'd'; SEM Micrograph of the Base metal at location 'e'; SEM Micrograph of the Stir zone at location 'f' from Figure 4-10.	53
Figure 4-13: Histogram showing the grain size distribution in the different zones.	54
Figure 4-14: Measured hardness map	56
Figure 4-15: Comparison of hardness in the top plate. The numbered data points correspond to the hardness map in Figure 4-14.....	57
Figure 4-16: Comparison of hardness in the bottom plate. The numbered data points correspond to the hardness map in Figure 4-14.....	58
Figure 4-17: Comparison of hardness in the vertical direction. The numbered data points correspond to the hardness map in Figure 4-14.....	58
Figure 4-18: Dimensions of the Tensile test specimen (mm).....	60
Figure 4-19: Machined tensile test samples.	60
Figure 4-20: Stress vs. strain curve for the as-received and the FSAM processed sample (2 mm hatch distance).	61
Figure 4-21: Tested FSAM processed sample after fracture	61
Figure 4-22: Dimensions of tensile shear test specimen (mm).....	63
Figure 4-23: Friction Stir lap weld sample and Tensile shear test specimen..	64
Figure 4-24: Tested lap weld sample.	64
Figure 4-25: Weld cross-section with the fracture location.	65
Figure 4-26: Close-up image of the hooking defect at location 'a' in Figure 4-25.	65
Figure 4-27: Weld macrostructure of 1 mm + 3.17 mm plates.	67
Figure 4-28: Weld macrostructure of 1.6 mm + 1.6 mm plates.	67
Figure 4-29: Close-up of defects from Figure 4-27.....	67
Figure 4-30: Close-up images of hooking and kissing bond defect from Figure 4-28.	68

Figure 4-31: Macrostructure of the addition of 1 mm plate to a 3.17 mm plate.	68
Figure 4-32: Macrostructure of addition of two 1 mm plates on a 3.17 mm substrate.....	68

ABSTRACT

Aluminum 6061 is extensively used in industry and welding and additive manufacturing (AM) of Al6061 offer flexibility in manufacturing. Solid-state welding and AM processes can overcome the shortcomings of fusion-based processes, such as porosity and hot cracking. In this thesis, friction stir welding and friction stir additive manufacturing, which are both based on the concepts of friction stir processing (solid-state), were studied. The welding parameters for a sound weld during friction stir welding of Al6061-T6 alloy were determined based on the experimental and numerical analysis. Formation of tunnel defects and cavity defects was also studied. A Coupled Eulerian-Lagrangian (CEL) finite element model was established to analyze the process, where the workpiece was modeled as an Eulerian body, and the tool as Lagrangian. The model was validated by conducting experiments and correlating the force measured by a three-axis dynamometer. The experimentally validated simulation model was used to find an optimum parameter set for the sound weld case.

To demonstrate the friction stir additive manufacturing process, a $40\text{ mm} \times 8\text{ mm} \times 8\text{ mm}$ (L×B×H) material was fabricated by adding five 1.6 mm thick plates. A similar coupled Eulerian-Lagrangian based finite element model was used to predict the effects of sound process parameters, such as the tool's rotational speed and the translational speed. The temperature predicted by the model was used to predict the microhardness distribution in the sample and to further elucidate the hardness change in the weld zone, which showed a good agreement with the experimental results. The microstructure of the samples was analyzed, and the mechanical properties of the additive manufactured samples were characterized and compared with those of other AM techniques via tensile tests and tensile shear tests.

1. INTRODUCTION

1.1 Motivation

Aluminum is the most abundant metal found on Earth. Aluminum alloy's various properties include high strength to weight ratio, high corrosion resistivity, high electrical conductivity, and formability. Owing to these various advantages, it is the second most used metal, after steel. Al alloys are considered useful and have found applications in many industries like transport, packaging, electrical transmission appliances, and architecture.

Al6061, a popular aluminum alloy is a relatively easy alloy to weld [1]. Popular fusion welding techniques such as metal inert gas (MIG) welding, tungsten inert gas (TIG) welding, gas metal arc welding (GMAW), and laser beam welding (LBM) are used to weld this material [2, 3, 4]. All welding processes lead to a reduction in mechanical properties. Fusion welding techniques lead to distortion and residual stresses, and its drawbacks related to melting and solidification include hot cracking, porosity, tearing, and voids due to shrinking. The heat-affected zone is larger owing to higher operating temperatures, and these coupled with undesirable microstructure in the weld zone require improvement in welding methods.

Solid-state welding processes, in particular, friction stir welding (FSW), overcomes a lot of fusion welding's limitations. FSW has shown its capabilities to make high strength welding joints, and can be used for welding different configurations as well as difficult to weld and dissimilar metals. FSW is a solid state welding process involving complex mechanisms and the defects (mainly volumetric) in FSW are related to its process parameters, and hence the strength of the weld depends on the process parameters. To find the welding parameters for a sound weld (free of defect) it is important to understand the physics of process, the temperature distribution and material flow. Numerical modelling offers a valuable tool in this regard and is cost effective compared to experiments. In this thesis, finite element modeling is employed to optimize the welding parameters to achieve a sound weld joint of Al6061-T6.

For alloys or metals that are difficult to join or weld, the whole part needs to be conventionally machined, which can be costly and wasteful. That is where additive manufacturing (AM) comes into play. AM is being used to fabricate functional parts, and AM of metals is now being used in many industries like medical, aerospace, and automotive. However,

aluminum alloys are very difficult to manufacture using laser-based additive manufacturing. The laser power required for melting the Al powders is high, owing to its high thermal conductivity and high reflectivity [5]. High oxidation in Al-based alloys hinders effective melting, and oxide causes further problems if it is entrapped in the molten pool. Due to the poor flowability of the Al powders, it is difficult to spread a thin layer of powder. The addition of some percentage of silicon improves these properties. That is why AlSi10Mg is the most commonly used Al alloy for AM. Al6061, on the other hand, a popular Al-Mg-Si alloy, is challenging to work with.

To overcome these shortcomings of laser-based additive manufacturing of Al6061, solid-state processes like friction stir additive manufacturing (FSAM) have been explored to achieve a better solution. The FSAM process takes the advantages of friction stir welding process into additive manufacturing of three-dimensional parts. This process is able to provide good metallurgical properties in the processed area, able to join many different materials, and could be used to manufacture large components. Use of friction stir process for additive manufacturing is relatively new and has not been studied much. Therefore, there is a strong need to systematically investigate FSAM of Al6061-T6 via modeling and experiments.

1.2 Background

1.2.1 Friction stir welding

Friction stir welding (FSW) is a solid-state welding process developed by the Welding Institute in 1991 [6]. Since then, there have been many research and developments on this topic in industry and academia [7, 8]. There are many advantages of this process, including excellent mechanical properties compared to other welding processes [7, 8]. It overcomes the disadvantages of fusion welding, such as porosity and hot cracking. It does not require specialized manual skill as it is an automated process. It is a clean, eco-friendly, and workspace safe process as it does not require the use of lasers, gases, or any radiations. It involves significantly less distortion owing to the lack of fusion and solidification.

The FSW process involves a non-consumable rotating tool plunging into the abutting edges of the plates or overlapping plates to be joined. The rotating tool creates localized heating and stirs the material. The heating is achieved by the friction between the tool and the workpiece, and the plastic deformation of the workpiece material. As the tool translates along the edge, the

material is deposited at the back of the tool and forms a joint. The side where the tool rotation is in the same direction of its translational velocity is known as advancing side (AS), while the other side where the tool rotation is in the opposite direction of the tool's translational velocity is known as retreating side (RS). The tool consists of two important features, namely, the tool pin and the tool shoulder. When the rotating tool is plunged into the plate, it softens the material and the tool shoulder helps in holding the material. The tool pin helps in stirring the material. Many advancements have been made in the development of the tool tip profiles and shoulder profiles to maximize the material stirring and eliminate any defects [9]. FSW can be thought of as a constrained extrusion process under the action of the tool. This process leads to very high strains and strain rates. This technique is called a solid-state process because the temperatures never reach the melting point. The temperatures achieved are around 60 % - 80 % of the melting temperature. This process leads to grain refinement in the stir zone (where the tool stirs the material). Equiaxed fine grains, as a result of dynamic recrystallization, are found in the stir zone. This grain refinement leads to more favorable mechanical properties, and the absence of melting of material alleviates the problems associated with solidification related defects.

The welding process consists of four phases: plunging, dwelling, welding, and pull-out, as shown in Figure 1-1. In the plunging phase, the rotating tool is lowered such that the shoulder of the tool is plunged into the workpiece (the depth depends on the tool, plate, and welding conditions). In the dwelling phase, the tool is stationary, the material is plasticized, and the local temperatures are raised. In the welding phase, the tool moves forward with a set speed, called welding speed, during which it mixes and stirs the material. The last phase is the pull-out phase, in which the tool stops and retracts from the workpiece. The FSW process leaves a pinhole after welding.

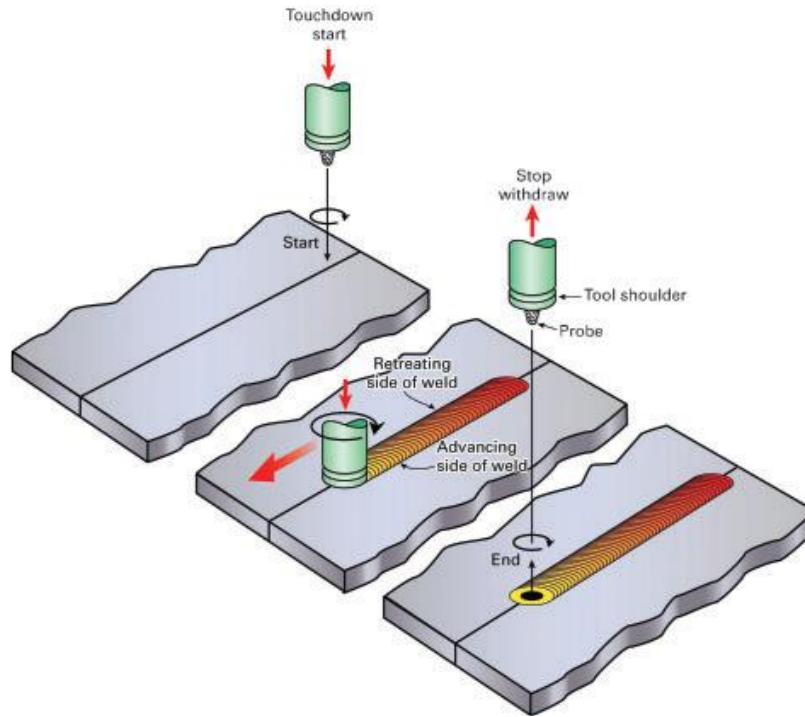


Figure 1-1: Welding schematic for Friction Stir Welding [8].

This technique is very flexible and can be used to weld a plethora of shapes in many different configurations like butt weld, lap weld, T-joint, spot weld. In addition to these, this technique has much versatility as it can be used to successfully weld dissimilar metals and metal matrix composites. In the case of lap welding, different aluminum alloys have been welded, like Al2024 and Al7075 [10, 11], Al5182, and Al6022 [12]. Aluminum alloys have been welded to magnesium alloys [13], aluminum alloys to steel [14], as well as magnesium alloys to steel [15]. Many studies have also been conducted on dissimilar butt welds [16-19].

The use of green, sustainable, eco-friendly metal joining processes, which can join even dissimilar metals with refined microstructure and good mechanical properties, makes it extremely useful in industry. It was used to replace fusion welds in Boeing's Delta II and Delta IV rockets [20], as well as to weld the frame of a business jet, the Eclipse 500, where this process replaced more than 7300 fasteners. Many ship vessels also use FSW for joining the structures. The cruise ship 'Seven Seas Navigator' used FSW to weld Al6000 series, Japan's 'Ogasawara' also used this welding process for its structure [8]. In the automotive industries, Honda used FSW to lap weld aluminum and steel parts for the engine cradle for the 2013 Accord [21]. This process helped them in making the vehicle light using light-weight materials and hence saving on

fuel consumption. Mazda employed friction stir spot welds to weld the sheets in the rear doors and aluminum bonnets of RX-8 [8]. Japan's high-speed train 'Shinkansen' used FSW to weld the Aluminum 6xxx frame because of its low distortion [8]. The weld was straight and up to 25 m in length.

1.2.2 Defects in friction stir welding

The defects in FSW are different from the ones observed in fusion welding as the welding is conducted in solid-state. The defects in FSW can be classified as surface and sub-surface defects. The surface defects are the ones that, like the name suggests, can be spotted on the plate's surface. There are two types of surface defects, namely, groove defect and excess flash. Excess flash is observed when the high heat is generated during the process. As a result, more material is softened, and it spews out of the tool shoulder on the retreating side in the form of flashes. Groove defects occur when the heat input is meager, that is, in the case of low rotational speed and high welding speed. Due to lower heat, the material is not plasticized, and forging action does not take place by the tool pin, thereby leaving a groove. Crawford et al. [22] found excess flash defects at higher rotational speeds such as 3750 rpm and 4500 rpm, keeping a constant welding speed constant at 1137 mm/min.

The sub-surface defects are the ones that occur underneath the weld surface. They are generally observed by looking at the weld's cross-section or by some non-destructive techniques such as X-ray radiography. The sub-surface defects are of many types: tunnel defects, cavity defects, and kissing bond defects. Tunnel defects or wormhole defects occur when the tool rotational speed is low. Lower tool rpm leads to colder welds, which implies less material softening and poor material flow. This defect leaves a void throughout the length of the weld. Reducing the heat input further gives rise to the groove defect discussed earlier. On the other hand, cavity defects occur when the tool rpm is sufficient, but the welding speed is too high. In this case, material softening is ensured, but the higher welding speed results in improper material deposition behind the tool, leaving a void. Kim et al. [23] reported the formation of cavity and groove defect when the welding speed was increased from 500 mm/min to 750 mm/min, respectively, keeping the rotational speed constant at 1500 rpm. Kissing defects usually occur in overlapping welds. They are generally oxide remnants between the adjacent edges of the plates

which remain unwelded due to severe shearing action and plastic deformation. Zhao et al. [24] observed kissing bond defects in every sample in their study of FSW of Al6013 in T-joints.

For a good quality weld with good mechanical properties, it must be defect-free. Most of the defects in FSW are related to the material flow or lack thereof. The material flow is dependent on hot or cold processing conditions, which are, in turn, affected by the process parameters. Figure 1-2 shows the effect of process parameters on weld quality. Optimum process parameters lead to the shaded area, which results in a sound weld. Therefore, it is imperative to find the optimum process parameters for a welding process.

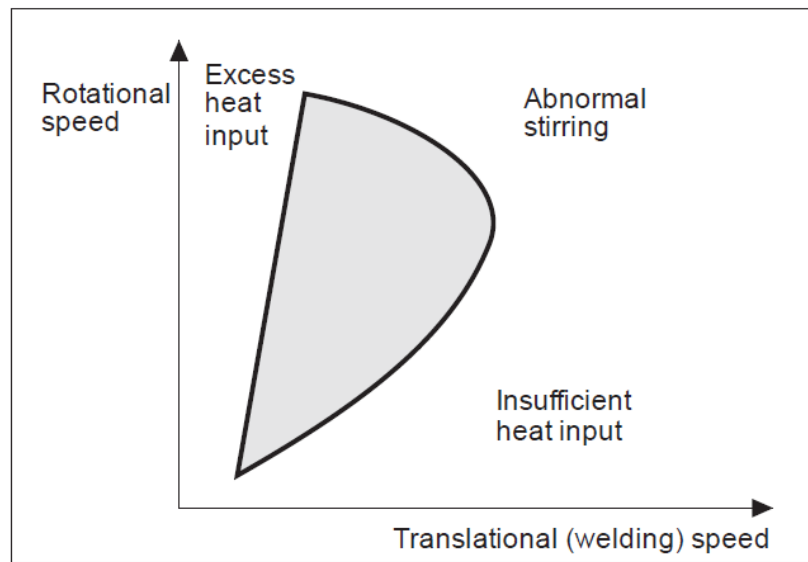


Figure 1-2: Effect of process parameters on weld defects [25].

1.2.3 Shortcomings of fusion-based additive manufacturing

Additive manufacturing (AM) refers to building components layer by layer. AM helps in manufacturing complex components with lesser waste. Fabricating intricate design and geometries and making lightweight parts help conserve material and energy consumption. AM also leads to a reduction in lead time, and inventory and helps speed up the supply chain [26]. Additive manufacturing of metals has found its application in the medical, aerospace, automotive industries. Metal AM has certain metallurgical differences compared to conventional machining such as mechanical anisotropy and residual stresses [27]. Some defects are specific to metal AM,

but as the technology is constantly evolving, it continues to address these topics. Different AM techniques are employed for different applications and materials. However, the most common commercially available techniques today are Powder bed fusion (PBF), Direct energy deposition (DED), sheet lamination, and binder jetting [28].

PBF, as the name suggests, is a powder-based technique. It includes selective laser sintering (SLS), direct metal laser sintering (DMLS), selective laser melting (SLM), and electron beam melting (EBM). PBF uses a high energy source (laser or electron beam) to sinter/melt the metallic powders on the powder bed to form one layer. Gong et al. [29] studied defects in SLS, EBM and SLM of Ti-6Al-4V. They reported that in PBF defects could be generated due to process parameter variability, fluctuations in electron or laser beam power, surface gas flow as well as the characteristics of raw materials. Grasso et al. [30] categorized the defects in PBF into porosity, residual stresses, cracking and delamination, balling, and impurities and microstructural inhomogeneties.

In the case of DED, metal powder or wire is injected, and a high energy source is used to melt it and deposit it on the substrate. Zhang et al. [31] studied the formation of surface pores in DED. They reported that the air entrapment led to the formation of bubbles which is detrimental to the performance and build quality of parts. Kies et al. [32] studied DED on high-manganese steel, and reported that insufficient shielding of gases resulted in oxidization which led to residual stresses and poor mechanical properties.

Both these techniques are fusion-based involving localized melting and evolution of microstructure based on solidification. Some defects observed were a result of solidification [33]. Porosities are a common defect in these techniques, occurred due to trapped gas in the power bed or due to insufficient melting. High thermal residual stresses are induced due to a high-temperature gradient, which accumulates as layers are added and cause distortion. Solid-state additive manufacturing techniques are used to overcome the disadvantages of fusion-based AM. Friction stir additive manufacturing (FSAM) holds promise in this regard by being a solid-state process with improving microstructure and structural performance.

1.2.4 Friction stir additive manufacturing

Friction stir additive manufacturing processes are based on the principles of friction stir welding and processing (FSW and FSP). It involves the use of a rotating tool with a special

shoulder and pin; it is used to plasticize the material and stir it. The transverse motion of the tool creates the length of the weld. Rotation of the tool, along with transverse motion, fills the plasticized material behind the tool. The main source of heat is the friction between the tool shoulder and the workpiece, as well as the heat generated due to plastic deformation [7]. The key parameters for the process are the tool rotational speed, and welding speed, with plunge depth, also playing a role. Since the material is stirred and deposited at higher temperatures but below the melting point, it is considered a solid-state process. The working temperature is usually between $0.6 \times T_m$ to $0.9 \times T_m$, where T_m is the melting temperature [7]. FSW/P locally modifies the microstructure of the material within the stir zone. It leads to the refining of the grain structure by producing ultra-fine grain structures as a result of dynamic recrystallization, which occurs due to high plastic deformation at elevated temperatures [34].

Refinement of microstructure coupled with its ability to weld difficult-to-weld and dissimilar materials makes it a very useful joining process. Hence, employing this technique to additive manufacturing opens up a new avenue for manufacturing. Some other advantages include lower thermal residual stresses due to relatively lower working temperatures, less energy consumption, better for the environment, and better load carrying capacity due to improved structural integrity and lack of defects.

1.3 Literature review

1.3.1 Numerical modeling of friction stir welding

Friction stir welding is a complicated thermo-mechanical process. Although the temperature in this process does not exceed the melting point, it is still high enough for the material to undergo some phase changes and changes in properties; that makes studying the thermal history important. Many studies have been conducted on developing numerical thermal models for FSW [35-37]. FSW is a thermo-mechanically coupled process where plastic deformation of the material is also a source of heat along with friction, and the amount of heat generated also controls the plasticizing of material. The main drawback of these models was not accounting for plastic deformation and thus resulting in underpredicting temperatures. Hamilton et al. [35] reported that their model predicted maximum temperatures over a wide range of energy input but under-predicted at lower energy input where plastic deformation dominates.

As mentioned in the previous section, in order to obtain a good quality weld, which is free of defects, it is essential to understand the material flow. In FSW, the material flow is dependent on the process parameters employed, like the welding speed, the tool rotational speed, the plunge distance (in case of displacement control), the axial force (in case of force control), or the tilt angle (if any). Some studies have used tracers or copper film in the workpiece to understand the flow of material around to tool [38, 39]. However, conducting such experiments is costly, and it also has its limitations in extracting detailed information such as temperature, stress, and strain distributions; that is why it is essential to develop fully coupled thermomechanical numerical models. With improved computational power, flow-based thermomechanical numerical models were developed and used to mimic the welding process. The numerical models can be classified into Computational Fluid Dynamics (CFD) and Computational Solid Mechanics (CSM). The two main formulation models used under CSM are Arbitrary Lagrangian-Eulerian (ALE) and Coupled Eulerian-Lagrangian (CEL).

Bendzsak et al. [40] developed a finite volume CFD model to visualize the flow around the tool. Colegrove and Shercliff [41] developed a 3-D CFD model to study the flow around a threaded tool. Their model however overpredicted the temperatures, as they assumed a sticking condition between the tool and the workpiece. The transverse welding force predicted by the model was an order of magnitude lower than the experimental one. The drawbacks of CFD models are that they cannot predict defects in the weld and they are usually based on the assumption of entirely sticking between the tool and workpiece and hence over predicted temperatures. It also could not include material hardening and material's elasticity.

Solid mechanics based thermomechanical finite element models have been used to study FSW. Dong et al. [42] developed one of the earliest thermomechanical FE models. They studied the physics of the FSW process assuming sticking condition, heat generation, and material flow, and reported that friction heating is dominant around the shoulder and the heat generation due to plastic deformation is mostly at the bottom around the pin. Ulysse [43] developed a fully coupled thermomechanical three-dimensional FE model. In this study, 'some slip' contact condition at the interface was assumed, and a good correlation between temperature history and tool forces was found. The study however did not deal with the defects formed in FSW.

The shortcomings of the finite element models and CFD models can be overcome by Arbitrary Lagrangian-Eulerian (ALE) formulation. It can be used to employ slipping contact

conditions and material's temperature dependence and hardening. Deng and Xu [44] developed a two-dimensional FE model assuming plain strain to study the material flow in FSW. Schmidt and Hattel [45] developed a three-dimensional fully coupled thermomechanical FE model using the ALE formulation, as this formulation enables large deformation and re-meshing. They used Abaqus/Explicit solver with the Johnson-Cook material law and Coulomb's friction law. They studied the plunging and dwelling action of the weld, in which the tool was assumed to be already in contact with the workpiece and submerging of the tool was not modeled as it would lead to excessive mesh distortion. They reported that higher heat dissipation from the workpiece led to a faulty weld with a void developing behind the tool. Zhang and Zhang [46] developed a 3D model using ALE. They reported that increasing the angular velocity improved the stirring in the stir zone and enhanced the weld quality. Zhang and Zhang [47] compared two contact models, namely, the classical Coulomb friction model and the modified Coulomb friction model, while simulating FSW. He found out that both models were satisfactory at lower tool RPMs, but only the modified Coulomb friction model was valid at higher tool RPMs. Zhang and Zhang [48] developed a thermomechanical model and studied the effects of weld parameters on material flow. They stated that when increasing welding speeds, tool rotational speed also needs to be increased to prevent voids.

Simulating FSW processes with ALE formulations is computationally expensive. Coupled Eulerian-Lagrangian (CEL) formulation is a computationally efficient way of modeling FSW processes. It also overcomes the limitation of ALE, which is its inability to characterize defects. ALE is represented by Lagrangian elements that need to be filled at all times. As a result, defects like cavities and voids cannot be simulated. They are just shown behind the tool as a lack of material deposition. CEL employs Eulerian and Lagrangian elements and can use the void layer in the simulation. Thereby enabling better prediction of defects and the process. Al-Badour et al. [49] developed a three-dimensional CEL FE model using Coulomb's friction law as the interaction between the tool and the workpiece. The model investigated the effects of the coefficient of friction, welding speed, and the plunging control method on the weld quality. The model predicted the voids in the welds and over predicted the forces on the tool while welding. They also reported that a lower coefficient of friction resulted in larger void sizes. Al-Badour et al. [50] also used a similar CEL FE model to simulate dissimilar metal welding between Al6061-

T6 and Al5083-O. They used various tool pin profiles and reported that the featured tool pin resulted in better weld quality.

1.3.2 Friction stir additive manufacturing

There are many different ways by which the friction stir process is employed to manufacture materials additively. One such technique is using a powder or a wire feeder developed by MELD manufacturing company [51]. This technique consists of a non-consumable rotating hollow tool with a shoulder, in which the metal powders or solid rod is fed. At elevated temperatures due to the heat generated and controlled high pressure, the feedstock material plasticizes and is deposited over the substrate for one layer. Subsequently, other layers can be added in which the bonding of the second layer will be over the first layer. It has been studied for the deposition of Al2219 and Inconel 625 [52 - 55].

Friction surfacing is another technique that uses a rotating consumable tool. An axial load is applied to the rotating tool, and at high temperatures due to the frictional contact, high plastic deformation occurs at the tool, and the consumable tool material is deposited on the substrate. By using optimal tool RPM, travel speed, and axial load, the thickness and the quality of the deposition can be controlled. Its primary application has been a coating of metals, but it has the potential to be used as an AM technique. The FSP process involving modification of a substrate by cold spraying metal powders on top of the substrate can also be employed as an AM technique [55]. This will involve spraying of the metal powders and using a non-consumable rotating tool to deposit the coating using the principles of friction stir processing. If this process is repeated layer by layer, a 3-D component will be built. The structure would have structural homogeneity, refined microstructure, and improved mechanical properties [55].

In this study, a technique of Friction stir additive manufacturing is studied in which a metal plate is added on top of the substrate by the use of a non-consumable rotating tool, as shown in Figure 1-3 [56 - 58]. Metal sheets are used as the feedstock material. The rotating tool with a special shoulder and tool tip is plunged in the top plate such that the tool tip enters the bottom plate. The two sheets under the tool undergo severe plastic deformation and are forged together. The rotating tool is made to travel along the desired path and hence, adds a sheet of metal on the substrate (or previous layer). The total height of the part is dependent on the thickness of the plates used and the number of the plates used. Post-processing might involve

some subtractive machining to obtain the final part. Being a solid-state process, it does not suffer from the problems related to solidification and porosity but leaves an equiaxed refined grain structure in the processed zone. Palanivel et al. [56] conducted an FSAM study on AA5083 and demonstrated line welds with build thickness of 11.2 mm. In another study, Palanivel et al. [57] demonstrated the FSAM fabrication of Mg-based WE43 alloy (Mg-4Y-3Nd) with a build thickness of 5.6 mm, and studied its microstructure and mechanical properties. Many studies on friction stir welding of Al6061 have been conducted [59 - 61], but little research on the use of FSAM on Al6061 is found.

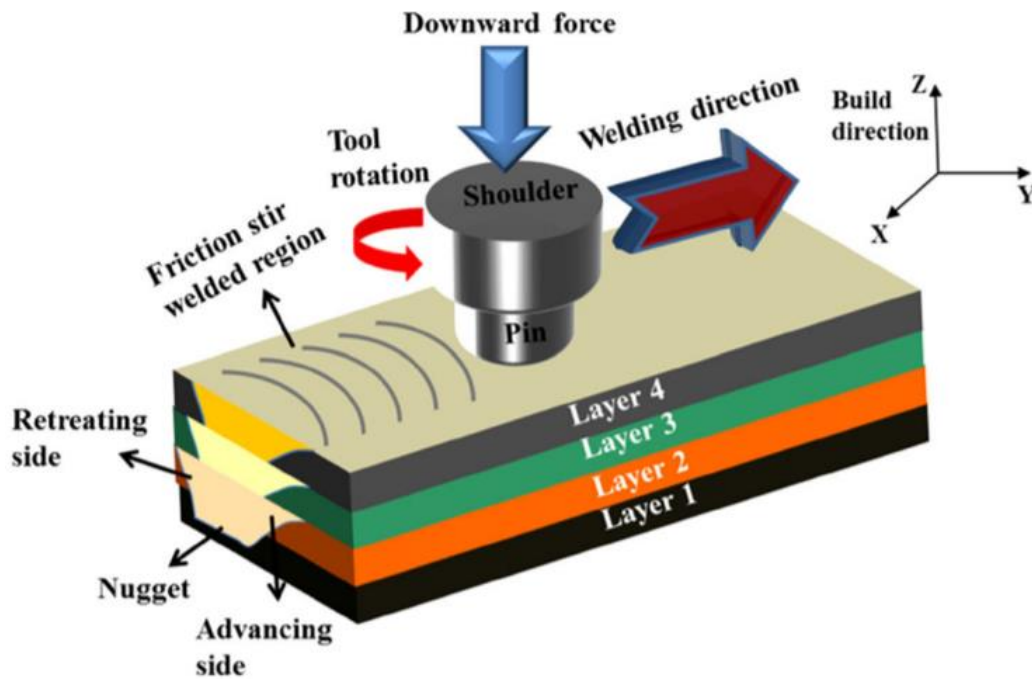


Figure 1-3: Schematic of Friction stir additive manufacturing [56].

1.4 Thesis objectives

From the literature study on the FSAM process, presented in the literature review section, it is found that there have been limited studies conducted on FSAM of aluminum 6061-T6, particularly in determining optimal conditions with minimum defects. In this study, the friction stir additive manufacturing process is studied on Al6061-T6. Like in FSW, the fabricated material's quality depends on the weld quality and being free of defects. The process parameters

for a particular tool and sheet dictate the type of defects or weld quality, as presented in [62]. The coupled Eulerian-Lagrangian based finite element model is modified for simulating additive manufacturing. The model is developed to predict the parameters for a sound weld for Al6061-T6. By expanding this model, this research will focus on further investigating friction stir additive manufacturing of Al6061-T6 via systematic modeling and experiments to gain further insights and predict the final resultant weld quality. The specific objectives of this study are:

- Developing and validating an FE Model for FSW and FSAM

In order to get a sound weld, optimum welding parameters need to be employed. In this study, a finite element model will be developed to explore the process parameters for a sound weld, and experiments will be carried out to validate the model and to investigate the damage. The model will also be expanded to simulate the friction stir additive manufacturing process, and predict temperature distributions, which will help in predicting material properties such as microhardness.

- Experimental investigation of friction stir additive manufacturing of Al6061

Experiments will be designed to systematically investigate the weld quality, microstructure and mechanical properties of the parts fabricated. Tensile tests will be conducted in the transverse direction to observe the strength and ductility. To measure the strength of the weld, tensile shear tests will be conducted. The microstructure of the processed part will be studied and used to explain the behavior of the material.

1.5 Thesis outline

The thesis focuses on developing a finite element model to predict the sound weld parameters for friction stir welding process and evaluating the effectiveness of friction stir additive manufacturing process. Chapter 1 deals with the introduction to the solid-state joining process topic, the motivation behind this study. This chapter also dives into the background of the process, defects related to FSW and provides a literature review of the numerical modeling of FSW, fusion-based AM techniques and FSAM. In addition, this chapter lays out the objectives of this thesis.

Chapter 2 provides details regarding the experiments conducted for both FSW and FSAM. This chapter talks about the experimental setup, the machine and tool used, the techniques used to prepare the sample, observe the microstructure, and the mechanical properties.

Chapter 3 presents the finite element model developed in this thesis to simulate friction stir processes, both FSW and FSAM. This chapter includes the model, assembly, interaction, material properties as well the boundary conditions employed. It also presents the results and the validation of the model against experiments.

The beginning of chapter 4 includes the results from the study on FSW, and explores the sound weld cases and the defects. The later part of the chapter consists of the results and discussions of FSAM study including, the microstructure observation, the microhardness comparison, the mechanical testing, and the defects. Chapter 5 concludes the findings of this thesis and provides the recommendation for future work.

2. EXPERIMENTAL SETUP

2.1 Friction stir welding setup

Friction stir welding was performed on 3.17 mm thick Al 6061 - T6 plates using Mazak VQC-15/40 vertical milling machine. A tool made of H13 tool steel was used with a tapered tri-flat threaded tool tip, the shoulder diameter of 6 mm, and the tool tip length of 2.1 mm. The pin diameter was tapered from 3 mm to 2 mm, as shown in Figure 2-1. The length of weld was 45 mm. The welding process consists of the plunging stage in which the tool moves at 12 mm/min to a plunge depth of 0.11 mm, a 5 second dwell, a pre-heat weld at 40 mm/min for 5 mm, and the welding stage at the set welding speed. A three axis Kistler 9257B dynamometer (connected to a Kistler 5004 amplifier) was used to measure the welding forces. A backing plate was used over which the aluminum plates were mounted. The backing plate served the function of heat dissipation from the aluminum plates. Figure 2-2 shows the experimental setup including the clamping fixture, the backing plate, the aluminum plate and the dynamometer.

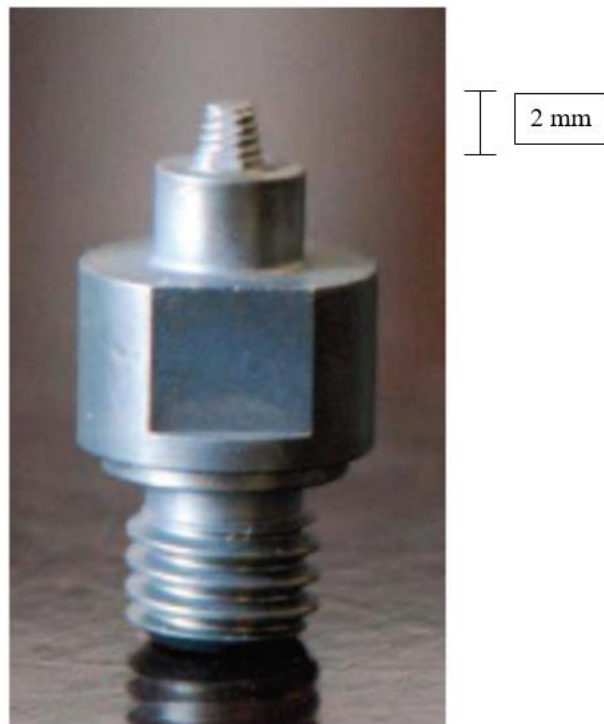


Figure 2-1: Friction stir welding tool.

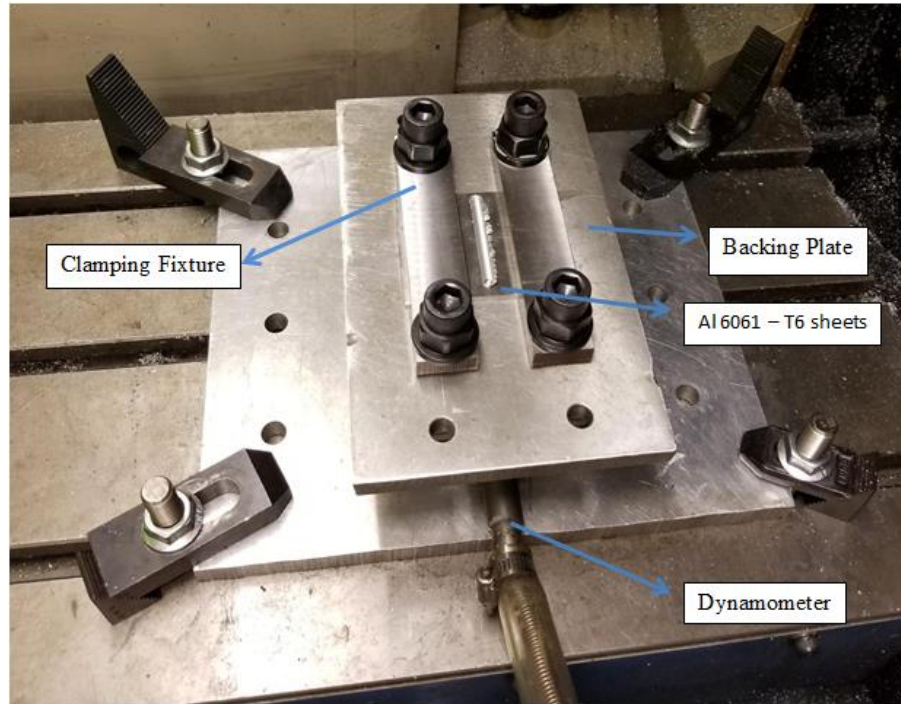


Figure 2-2: Friction stir welding setup.

2.2 Friction stir additive manufacturing setup

The experimental setup consisted of a 1.6 mm Al6061 plate mounted on the top of another 1.6 mm Al6061 plate. Like in FSW experiment, an aluminum backing plate was used to facilitate heat transfer from the workpiece. The same tool is used for this experiment as well. The Mazak VQC-15/40 vertical milling machine was used for the friction stir additive manufacturing experiment. The process comprised of plunging of the rotating tool into the workpiece at a speed of 12 mm/min to a plunge depth of 0.11 mm, and a five second dwell time to heat up the material, followed by a preheat weld at 40 mm/min for a distance of 5 mm. The welding process at the process parameters of 1800 rpm and 125 mm/min was then performed. Like in FSW, the welding forces were measured with the help of a three-axis Kistler 9257B dynamometer connected to a Kistler 5004 amplifier. The experimental setup is shown in Figure 2-3.

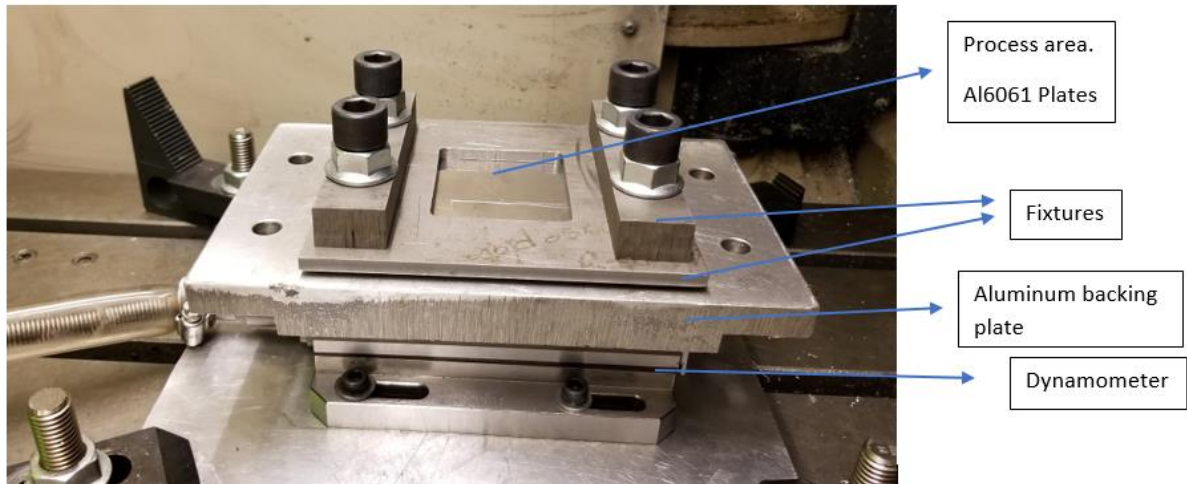


Figure 2-3: Experimental Setup for Friction stir additive manufacturing.

After the first plate is added, the excess flashes and burrs are removed and the next plate is mounted on the top. The process can be repeated to add more plates, and hence build more layers. The total thickness of the part is dependent on the thickness of the plates and the number of plates. In this study an area of $8 \text{ mm} \times 40 \text{ mm}$ was processed as shown in Figure 2-4. This was carried out by making four passes of the tool at a separation of 2 mm. Five 1.6 mm Al6061-T6 plates have been added to the substrate. Figure 2-5 shows the FSAM part after post-processing. Figure 2-6 shows the transverse cross section of the sample. For testing the mechanical strength of the sample produced, two 1.6 mm plates were added together and a tensile test was conducted to evaluate the material properties. A processed area was added, from which the tensile specimens were cut as presented in later sections. In order to test the joint strength, a tensile shear test was conducted by making a shear test sample. Microhardness tests were conducted on the sample by using a 200 g load, a dwell time of 15 seconds, and a diamond indenter as per ASTM standard E384 [63]. Addition of another set of plates was studied in which 1 mm thick plates were added to 3.17 mm thick substrate. Both the plates were Al6061-T6. The second case will be discussed in the defects section.



Figure 2-4: The top view of the weld adding 5 plates on the substrate.



Figure 2-5: The FSAM part.

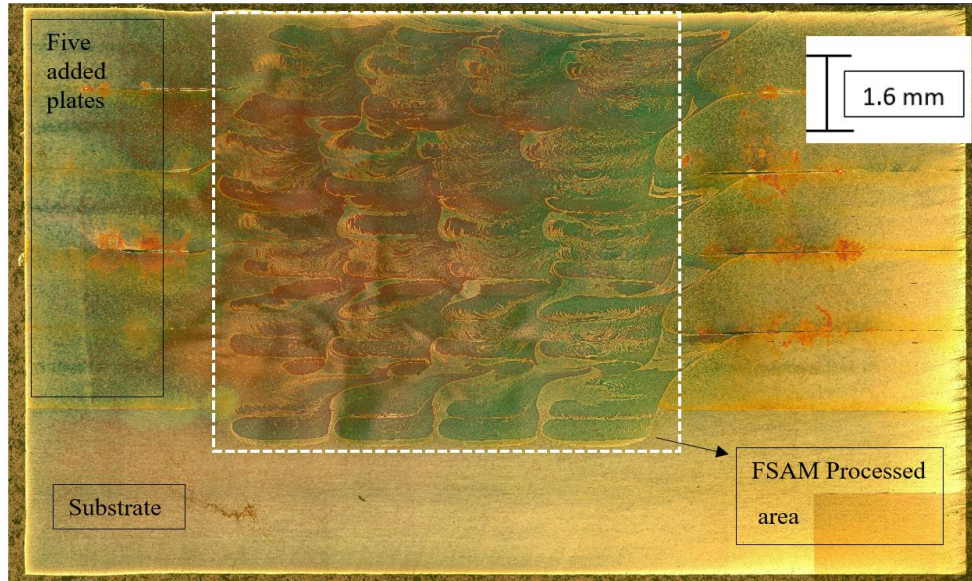


Figure 2-6: The cross-section of the FSAM processed area.

2.3 Sample preparation and mechanical testing

To observe and study the microstructure and the weld cross-section, the samples were prepared as per ASTM standard E3 [64]. The samples were sectioned transversely, hot mounted on Bakelite and then ground with 180, 400, 600, 800, and 1200 grit grinding wheels. The samples were then polished with 6-micron, 1-micron and 0.1-micron diamond paste, and then colloidal silica. To observe the weld macrostructure, the samples were etched with Caustic solution for 10 minutes. To observe the microstructure, the samples were immersed in Weck's reagent (4% potassium permanganate and 1% sodium hydroxide) for 20 seconds. The microstructure was observed in a Nikon Eclipse LV150 optical microscope and a JEOL JSM-T330 scanning electron microscope.

For tensile testing of the specimen, two 1.6 mm plates were added on top of each other. The dimensions of the tensile test specimen were as per ASTM standard B557M for a subsize specimen [65]. The testing was carried out with strain control till yield at 0.5%/min and position control at 1.27 mm/min until failure. For the tensile shear tests, lap weld samples were fabricated. ASTM D1002 standard was used to determine the width of the testing specimen, and the testing speed used is 1.3 mm/min [66].

3. FINITE ELEMENT MODEL

In this study, a coupled Eulerian-Lagrangian (CEL) based FE model is used. CEL formulation makes the visualization of the process easy and it makes it possible to view the voids and hence the defects. Good agreement between the axial forces, temperature evolution, weld condition is observed.

3.1 Friction stir welding

3.1.1 Model, Assembly, Mesh and Material Properties

The domain size of 20 mm \times 20 mm was considered in this study, which is four times the shoulder diameter of the tool. The domain thickness was the same as that in the experiments, i.e., 4.17 mm with 3.17 mm being the thickness of the workpiece and the 1 mm being the thickness of the void layer. The additional 1 mm void layer was defined at top of the workpiece to incorporate flash formation during FSW. The workpiece was modeled using Eulerian elements as it can simulate both voids and material. The tool and backing plate were modeled as a Lagrangian body. An aluminum backing plate was modeled to simulate the heat transfer from the workpiece. The H13 tool steel tool used in the study is defined as a rigid isothermal Lagrangian body. Al Badour et al. [49] compared the formation of volumetric defects by using a featured and a featureless tool pin profile and claimed a featureless tool pin profile was not able to predict a sound weld case. The featured tool pin profile facilitates higher material mixing and generates more plastic flow. It helps in predicting the sound weld case (with no defects). In this study, a featured tool tip was used, and the tool tip was tapered and consisted of flats, as shown in Figure 3-1. The dimensions of the tool were similar to the one used in the experiments.

The FSW tool was modeled as a rigid isothermal Lagrangian body and was meshed with 15372 C3D8RT elements. Biased meshing is used as shown in Figure 3-2, where the tool is in direct contact with the workpiece to improve accuracy and reduce computational time. The Eulerian workpiece was meshed with 160,000 EC3D8RT elements. The Lagrangian backing plate with same dimensions as the workpiece and 2 mm thickness was meshed with 25600 C3D8RT elements.

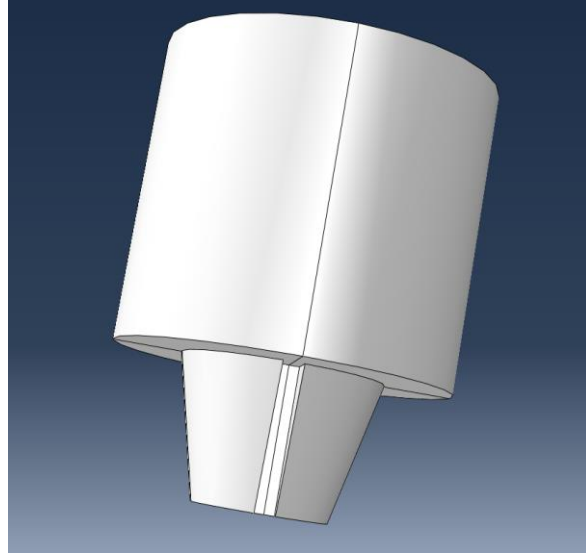


Figure 3-1: The featured tool used in the simulations.

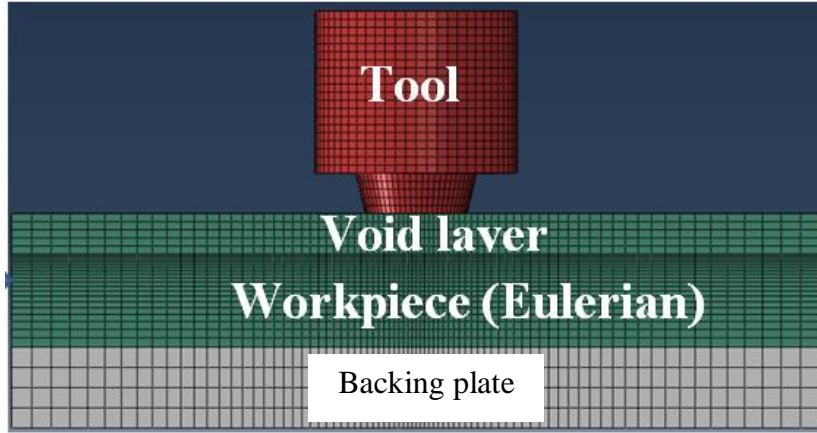


Figure 3-2: Assembly and mesh used in the FE model.

Temperature-based elastic and thermal properties were defined for the workpiece (Al6061-T6). The properties could be found in [49]. The Johnson-Cook plasticity model for Al6061 is given by:

$$\sigma_o = [A + B(\bar{\epsilon}^{pl})^n][1 + C \ln\left(\frac{\dot{\bar{\epsilon}}^{pl}}{\dot{\epsilon}_o}\right)](1 - \hat{\theta}^m),$$

where $\bar{\epsilon}^{pl}$ is the equivalent plastic strain, $\dot{\bar{\epsilon}}^{pl}$ is the equivalent plastic strain rate, $\dot{\epsilon}_o$ is the normalizing strain rate, which is usually 1 s^{-1} , and $\hat{\theta}$ is the nondimensional temperature defined as $T - T_{ref} / T_{melt} - T_{ref}$. The temperature-dependent material properties, and the Johnson Cook material parameters - A, B, C, n, m are provided in Table 3-1.

Table 3-1: Johnson Cook material parameters for Al6061.

A (MPa)	B (MPa)	C	n	m	T _{ref} (°C)	T _{melt} (°C)
324	114	0.002	0.42	1.34	24	583

3.1.2 Contact, Interactions and Boundary conditions

The contact condition used between the tool-workpiece interface is defined by Coulomb's law of friction. Schmidt and Hattel [45] reported that it is an accurate way of modeling contact condition at the tool-workpiece interface in friction stir welding. Separation is allowed between the tool-workpiece to simulate FSW process accurately and predict the welding parameters for sound weld case and defects. In Abaqus, tangential behavior is used with penalty contact formulation. Al-Badour et al. [49] with the help of this contact condition, were able to model defects in friction stir welding of Al 6061-T6 and validate against the experimental results. In this study, the friction coefficient was fine-tuned in the FE model till good agreements with experimental force and temperature results were achieved, as used by Al-Badour et al. [49] to identify the suitable friction coefficient in their FE model. It was observed that as the tool rotational speed increased, the friction coefficient increased as well. A similar phenomenon was observed by Kumar et al. [67] and his paper gives a detailed explanation for the increase of friction coefficient with tool rotational speed. In this study, the coefficient of friction at the tool—workpiece interface was set as 1.2 for 2000 rpm. The model was also used to predict the defects, at 1200 rpm, coefficient of friction of 0.95 was used.

To simulate the heat transfer from the plates to the backing plate, a pressure-based contact conductance was used between the workpiece and the heat sink. The model is defined by:

$$q = k_p(\theta_c - \theta_d)$$

where q is the heat flux per unit area, k_p is the contact pressure-dependent contact conductance, θ_c and θ_d are the surface temperatures of the workpiece and backing plate respectively, in contact with each other. The value of k_p is set as linearly varying from 3000-4000 W/m²K, as suggested by Soundararajan et al. [68] for contact pressure varying from 0 - 12.5 MPa. General contact formulation was used establish contact between the different surfaces, such as tool-workpiece and workpiece-backing plate.

The boundary conditions applied to the workpiece were velocity based. The welding speed was defined as material velocity in one direction, and the velocity constraints were applied in the other two sides to prevent the material from side spreading, as shown in Figure 3-3. The tool rotation was applied to the rigid tool. The tool plunge in the workpiece was kept as the same in the experiments, which was 0.11 mm. Table 3-2 shows the welding parameters used in this simulation with the coefficient of friction used. The main focus of this study was to develop a model to predict sound weld cases, but two other cases in which defects were formed are also shown.

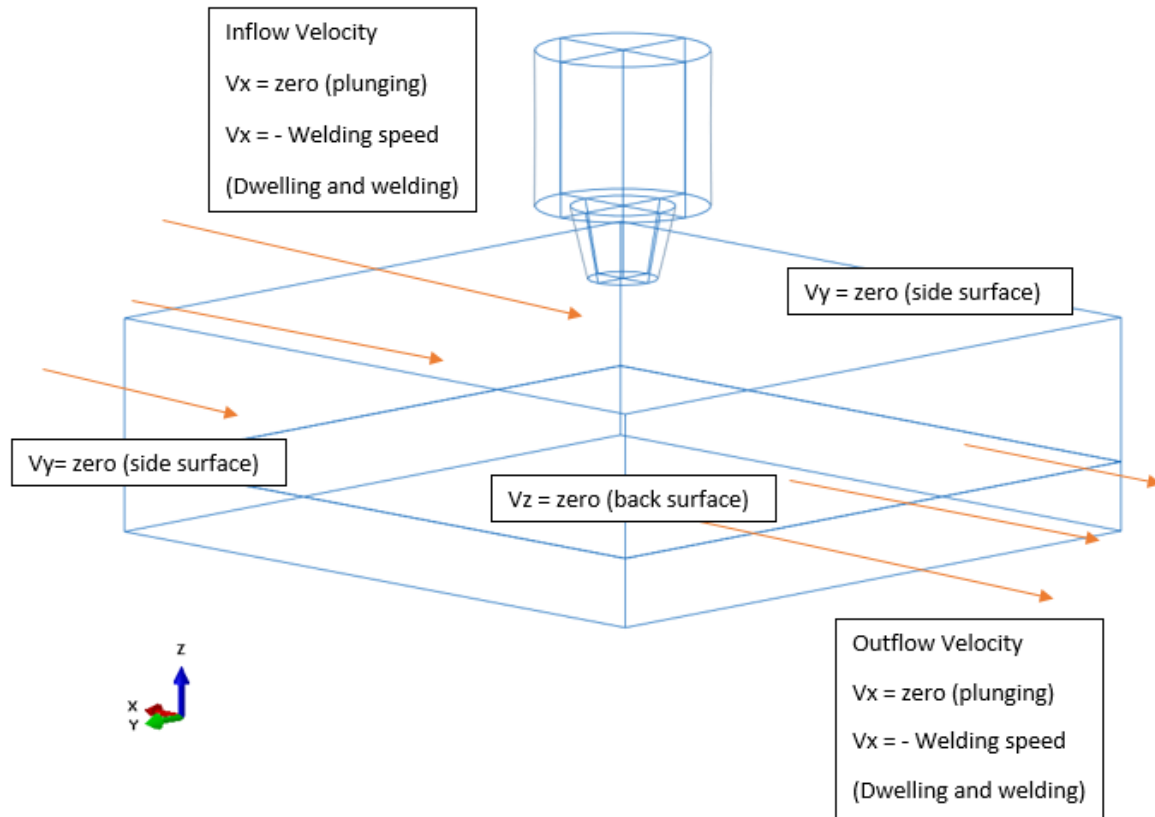


Figure 3-3: Boundary conditions employed in FSW simulations.

Table 3-2: The experimental and simulated parameters of the welding cases.

Case	Tool RPM	Weld Speed (mm/min)
1 (Sound Weld)	2000	200
2 (Tunnel Defect)	1200	300
3 (Cavity Defect)	2000	400

3.1.3 Model validation

In this study, the FE model was first developed as discussed in the previous section. Experiments were then performed to check if the FE modeling results could match the experimental results. After performing multiple simulations, the friction coefficient as mentioned in the previous section, was determined to be 1.2 for 2000 rpm and 0.95 for 1200 rpm. Using this coefficient of friction at the tool workpiece interface, a good comparison was achieved between

the simulation and experimental results as shown in **Error! Reference source not found..** Figure 3-4 shows the comparison of experimental and simulation results of the axial force for the welding process for case 1. The process parameters that produced a sound weld were 2000 rpm and 200 mm/min, as determined both experimentally and in the FE model. As shown in Figure 3-5 the weld nugget formed experimentally shows a good agreement with the weld nugget predicted by the simulation. It was then observed that when the tool rpm was reduced with tool velocity increasing (1200 rpm and 300 mm/min), tunnel defects were formed in the advancing side of the weld. In the third case when the tool rpm was set at 2000 and the tool velocity was increased to 400 mm/min, it resulted in the formation of cavities, which were observed in the advancing side of the weld.

Table 3-3: Comparison between the measured experimental axial forces and the simulated axial forces.

Tool rpm (RPM)	Tool speed (mm/min)	Mean Exp. Steady state forces (N)	Mean Predicted Steady state forces (N)	Relative Error (%)
2000	200	2076	2142	3.2
1200	300	3533	3761	6.5
2000	400	2725	2952	8.4

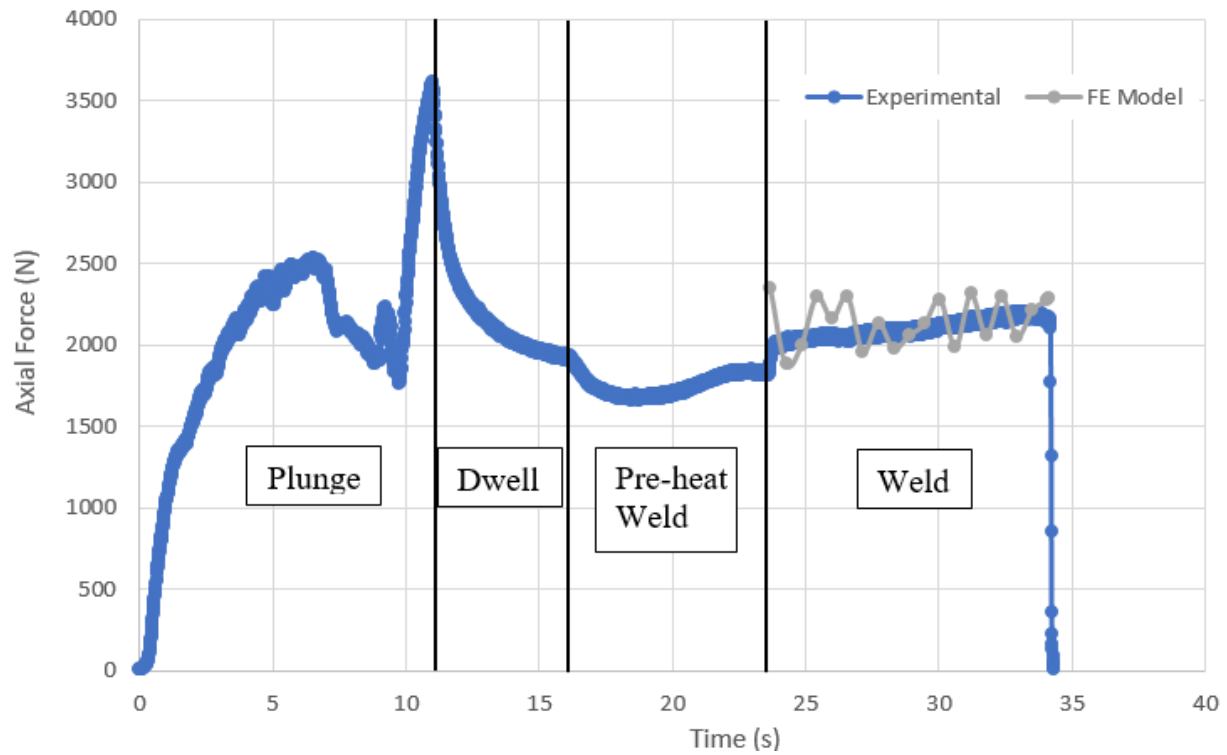


Figure 3-4: Plot comparing of experimental axial force and simulated axial force.

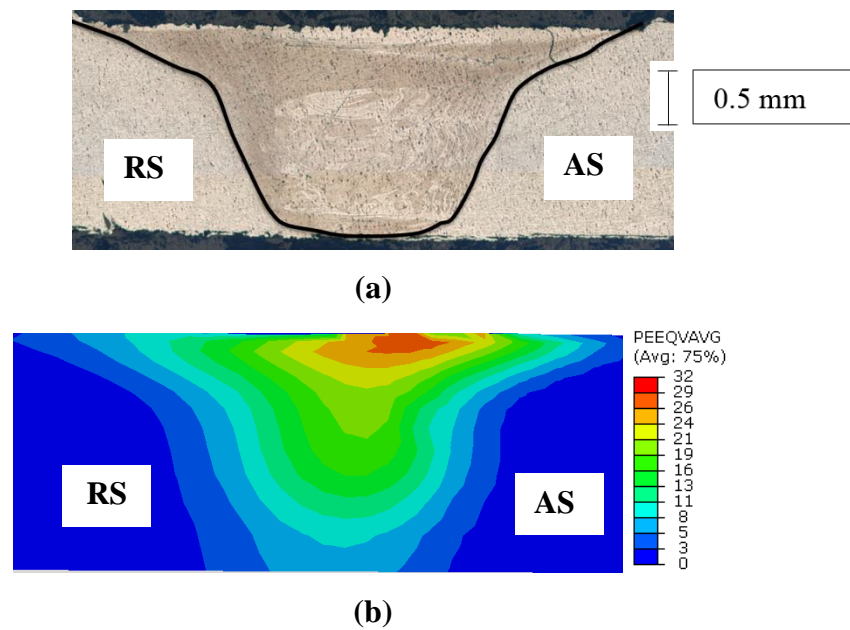


Figure 3-5: Experimental stir zone (a); Simulated stir zone (b).

3.2 Friction stir additive manufacturing

The finite element model used in the study of FSAM is similar to the one used for FSW with few changes to the assembly, contact properties and boundary conditions.

3.2.1 Model, Assembly, Mesh and Material Properties

The domain size of the model used is the same as the one used in FSW simulation, i.e., 20 mm × 20 mm. For the purpose of studying additive manufacturing, two plates are stacked on top of each other. In the model, the two plates are modeled with a partition in between. The thickness of each plate is the same as that used in the experiment, i.e., 1.6 mm. The total thickness of the domain is 4.2 mm, including a void layer, which is 1 mm thick. The void layer is to incorporate the flashes during the process. The model assembly is shown in Figure 3-6.

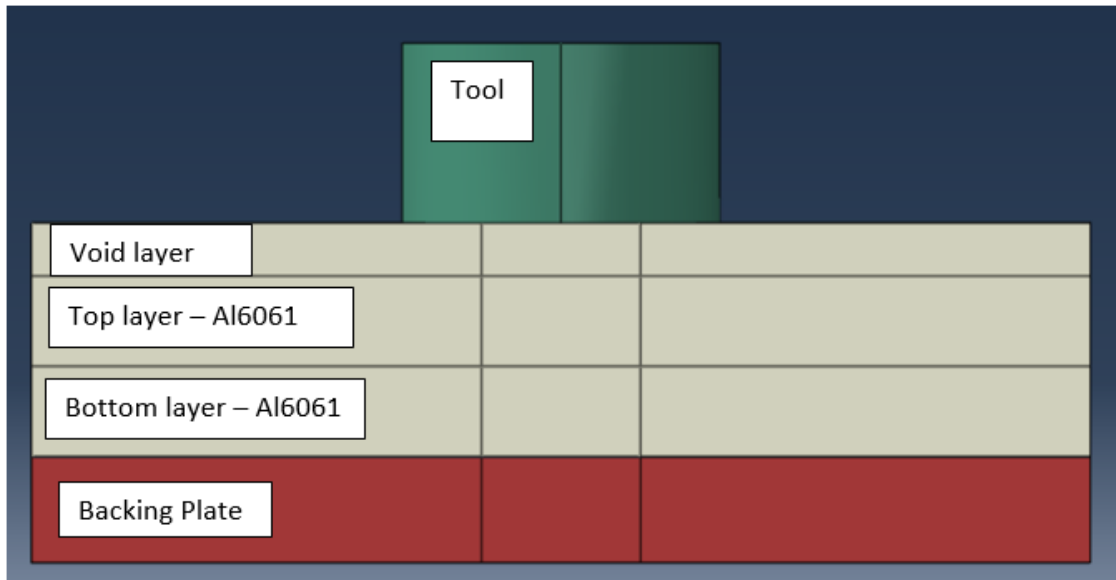


Figure 3-6: Assembly of the FE model.

Since the same tool used for FSW experiments is used for FSAM experiments, the same featured H13 tool steel tool is used in this FE model as well. The Lagrangian tool was meshed with 10142 8-node thermally coupled brick elements - C3D8RT elements. The Lagrangian backing plate was meshed with 5184 C3D8RT elements. The Eulerian workpiece was meshed with 24624 8-node thermally coupled linear Eulerian brick elements - EC3D8RT elements. To ensure high accuracy and lower computational time, biased meshing was used in this study with

finer meshes employed near the contact, like the previous model. Since FSAM is studied on the same material, i.e., Al6061-T6, the material properties used in this model were the same as that used in the FSW model.

3.2.2 Contact, Interactions and Boundary conditions

The boundary conditions applied to the workpiece were velocity based, same as in the case of FSW. The boundary conditions are shown in Figure 3-7. The tool plunge in the workpiece was kept as the same in the experiments, which was 0.11 mm. The interaction between the tool and workpiece was defined using a general contact formulation, which was modeled by Coulomb's law of friction with the friction coefficient of 1.2 without allowing separation.

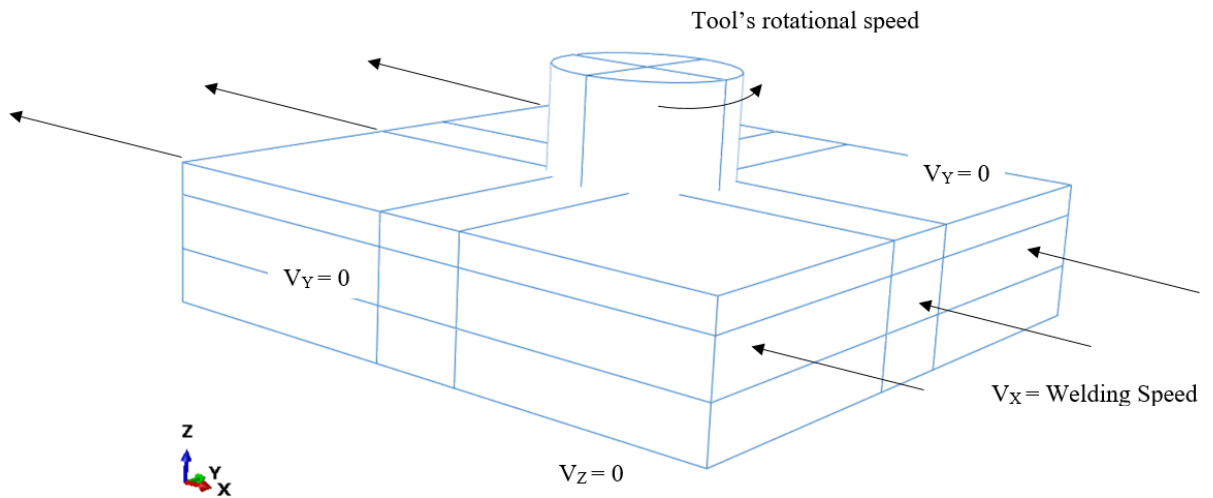


Figure 3-7: Boundary conditions for FSAM simulations.

To simulate the heat transfer from the plates to the backing plate, a pressure-based contact conductance was used between the workpiece and the heat sink, same as in the case of FSW. The range of contact conductance used was 15000 – 30000 W/m²-K [69]. Individual contact property assignment was used under general contact to assign properties for the tool-workpiece interface and the workpiece-backing plate interface.

Since two plates are mounted on top of each other, to model the heat transfer between the two plates, a thin section of material with low thermal conductivity was introduced. As the workpiece is an Eulerian part, a contact interaction property assignment between the plates cannot be used to simulate the effect of the interface.

As mentioned before, in this study, to simulate the effect of interface between the two plates, a thin section of material with low thermal conductivity was introduced. The thermal conductivity was varied from 20 W/m-K to 35 W/m-K based on the contact conductance values presented by Yeh et al. [69], who calculated the contact conductance at different contact pressures for Al-Al plates joined by bolts. This approximates the heat lost due to the contact resistance and helps in predicting the hardness of the plates, as discussed in the later sections.

3.2.3 Model validation

As can be observed from FSW studies, improper process parameters lead to defects in the friction stir processes. For a given tool, the welding speed and tool rotational speed (RPM) dictate the quality of the weld. Ajri et al. [62] described the influence of the welding parameters on the defects. If the tool RPM is too low, there is insufficient heat generation; if the welding speed is too high, there is abnormal stirring; and if the welding speed is optimal, but the tool RPM is high, there is excess flash. Hence, this finite element model is developed to simulate the FSAM process and to predict the process parameters for a sound weld. Like in the case of FSW, to validate the finite element model, the axial forces were compared to the measured values from the experiment, along with the stir zone, which was compared by juxtaposing the weld macrostructure with the equivalent plastic strain from the simulation. Figure 3-8 shows the plot of axial forces vs. time as measured by the dynamometer in comparison with the predicted axial forces only during the welding process because the steady state welding process is what affects the joint strength and resultant microstructure. The mean axial force measured during the welding phase of the experiment was 1949.57 N, and the mean axial force predicted by the FE model was 1988.42 N. The values were close with an error of 2%. The coefficient of friction used in the model was 1.2. Figure 3-9 shows the stirred zone as predicted by the model while simulating friction stir additive manufacturing of a 1.6 mm plate on a 1.6 mm plate, which shows a good agreement with the experimentally identified stir zone.

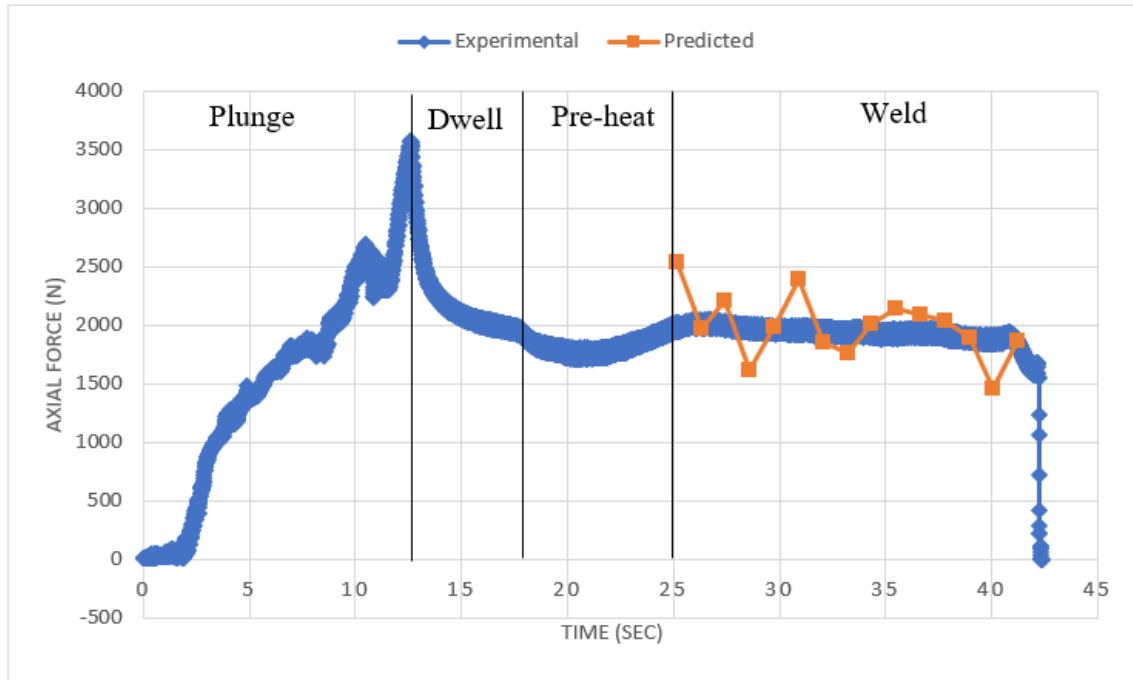


Figure 3-8: Comparison of Axial Forces between Experiment and FE model.

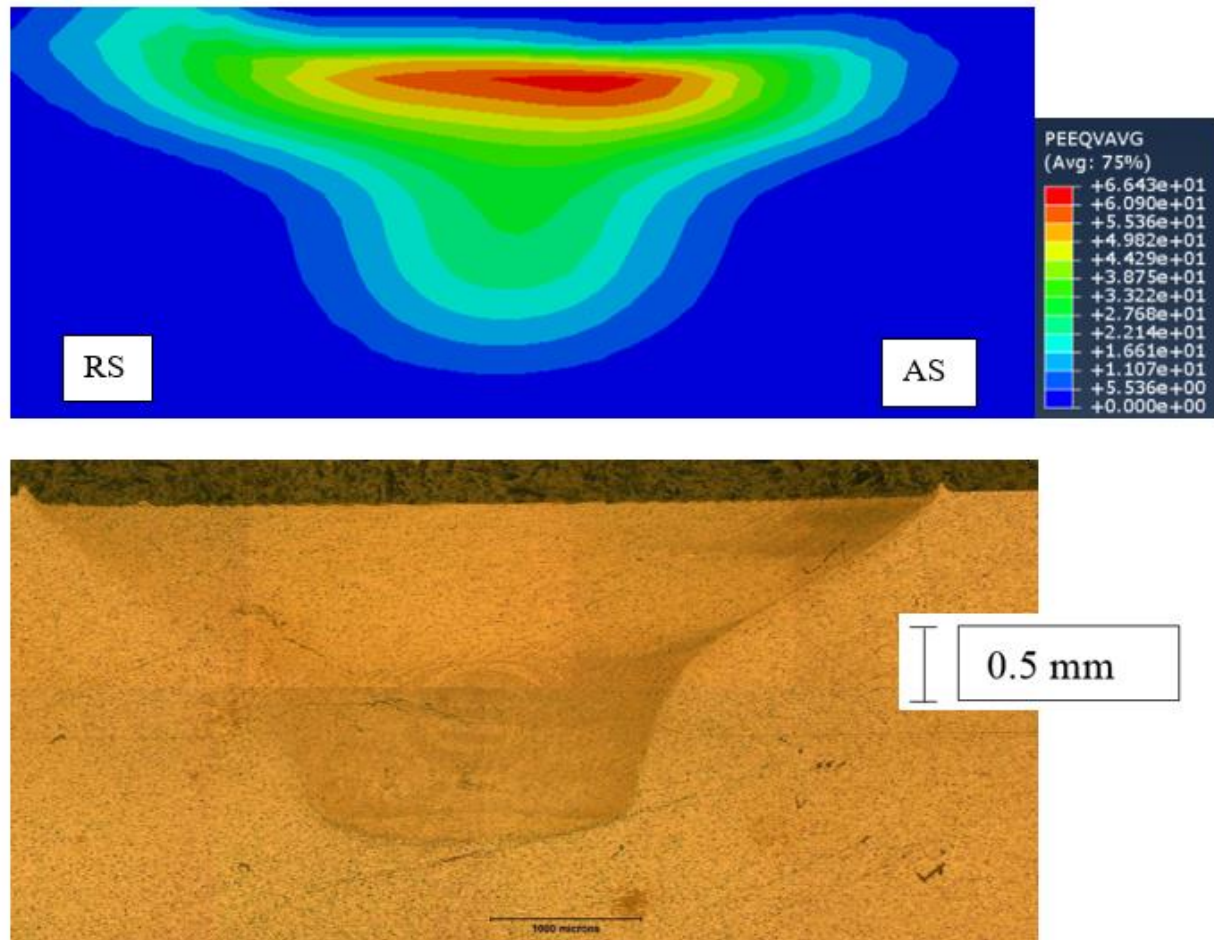


Figure 3-9: Comparison between the experimental stir zone and the simulated stir zone.

4. RESULTS AND DISCUSSIONS

4.1 Friction stir welding

4.1.1 Sound weld

A sound weld case is observed when the conditions, such as the rotational speed and the welding speed, are optimum. During this process, the temperature is below the solidus melting point of the material and it is beneficial for the stirring action. In this study of FSW, sound welds were observed at tool's rotational speed of 200 rpm and welding speed of 200 mm/min.

The temperature observed in this case was not as low as in the case of tunnel defect formation. The optimal rotational speed of the tool was able to plasticize the material and the optimal welding speed ensures deposition of the material behind the tool. Also, there does not exist any gap between the tool pin driven flow and the shoulder driven flow, as seen in Figure 4-1, where the top left pointing blue arrow represents the shoulder-driven flow and the down left pointing orange arrow which represents the pin-driven flow. The temperature distribution at the cross-section is nearly symmetric, as shown in Figure 4-2. By increasing the tool rotational speed, high temperatures are achieved, hence more material softening, which leads to the formation excess flashes in the RS.



Figure 4-1: Sound weld cross-section (at the center of the model). (Top left pointing blue arrow-shoulder-driven flow; down left pointing orange arrow- pin-driven flow).

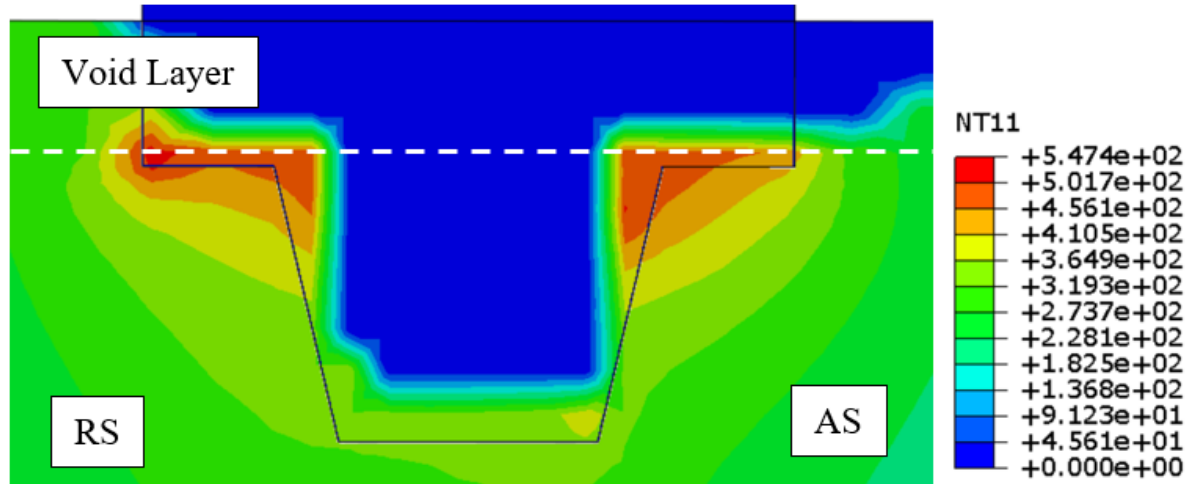


Figure 4-2: Temperature distribution around the tool during sound weld formation.

4.1.2 Defect formation in FSW

As mentioned before, the main focus of this thesis was to predict the sound weld case. However, to show that the model was capable of predicting defect at certain welding parameters, two defects were explored namely, tunnel defect and cavity defect. The following sub-section would talk briefly about the formation of defects as predicted by the FE model.

Tunnel defect

Formation of tunnel defects occur at lower rotational speeds of the tool. At lower rotational speeds, higher temperature which are conducive to stirring are not reached, as there is less heat generation. As a result, there is less material softening and hence less plastic flow. A temperature of around 80 % - 90 % of the solidus temperature, which is around 450 °C – 550 °C for Al6061-T6, is conducive to proper stirring. In the case of this defect, the peak temperature reached was around 400 °C in RS, as seen in Figure 4-3. In FSW, the material flows from the RS to AS, lower temperatures in the RS (around 350 °C) mean that there is insufficient forging at the AS and hence defects appear on the AS, as seen in Figure 4-4. Higher temperature at the tool shoulder suggests that the shoulder is able to forge the material on the AS. However, since the temperatures at the tool pin are much lower, there is much less plastic flow, hence, a void is left behind. Figure 4-4 shows the void fraction at the cross-section in the workpiece, where the red

region represents a void (EVF_VOID = 1) and the blue region represents material (EVF_VOID = 0).

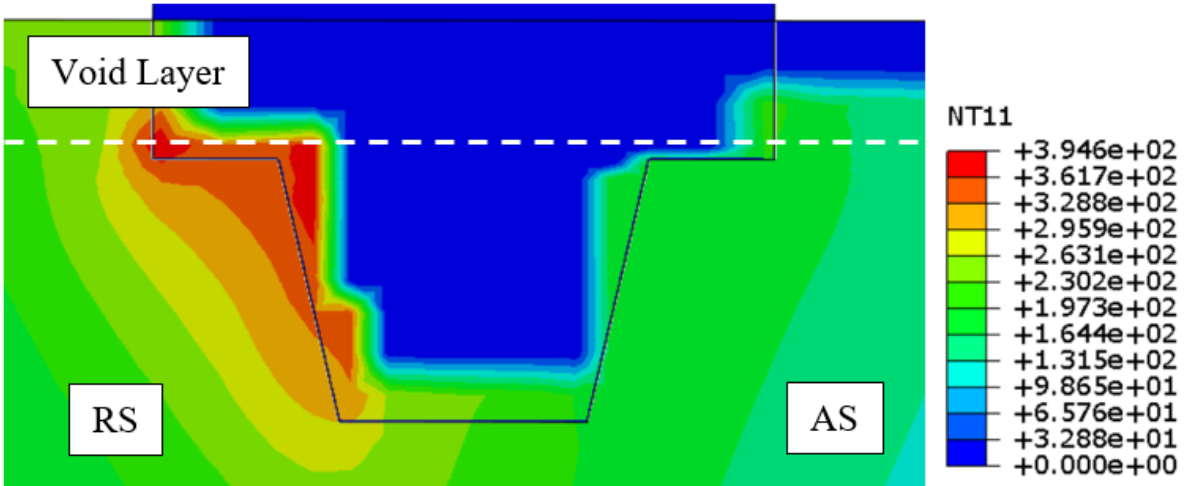


Figure 4-3: Temperature distribution in the case of tunnel defect.

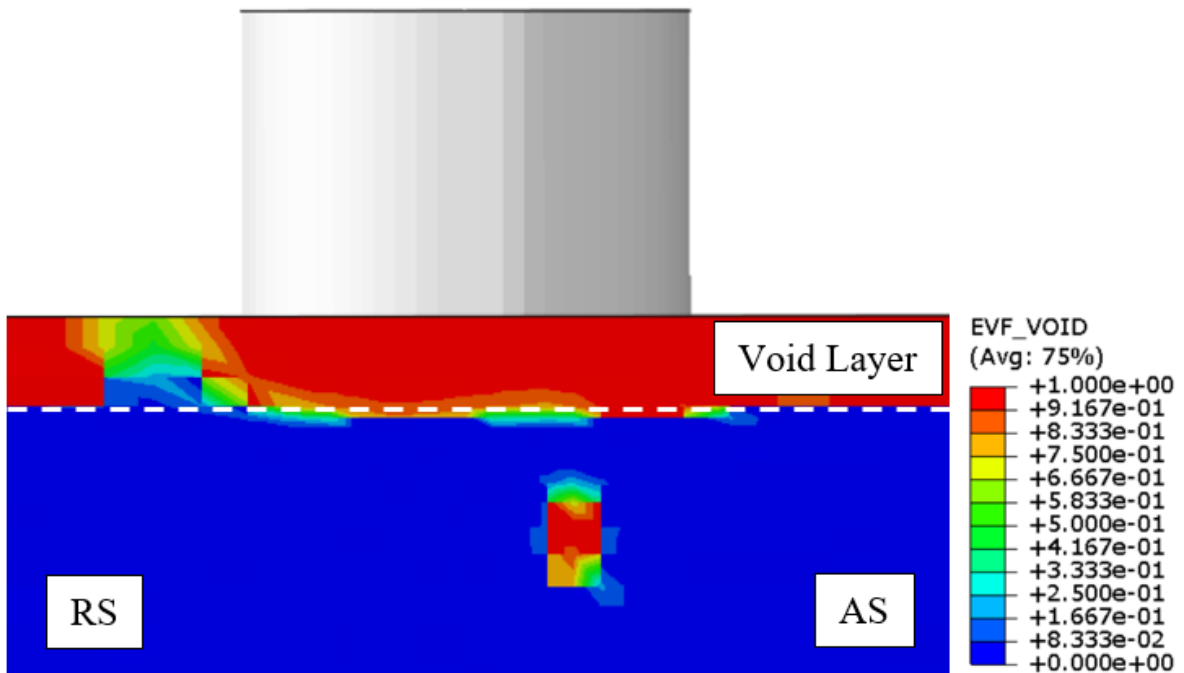


Figure 4-4: EVF_Void distribution in the case of Tunnel defect. A void is noticed at the advancing side.

Cavity defect

Formation of cavity defects occur at higher welding speeds. Higher or optimum tool rotational speeds ensure that the temperature in the workpiece is high enough to soften the metal, as seen in Figure 4-5. However, due to higher welding speeds insufficient stirring takes place and material fails to deposit behind the tool. There exists a gap in between the shoulder driven flow and the tool pin driven flow, which leads to the formation of voids. Figure 4-6 shows the void fraction at the cross-section in the workpiece, where the red region represents a void (EVF_VOID = 1) and the blue region represents material (EVF_VOID = 0).

By decreasing the energy input, such as by either reducing the tool rotational speed or increasing the welding speed, defects occur in FSW processes. If the welding speed is further increased, the cavity defect results in a groove defect where, where material behind the tool is not deposited. Kim et al. [23], studying FSW in ADC12 aluminum die casting alloy, reported the formation of groove defect when the welding speed was increased from 500 mm/min to 750 mm/min respectively, keeping the rotational speed constant at 1500 rpm.

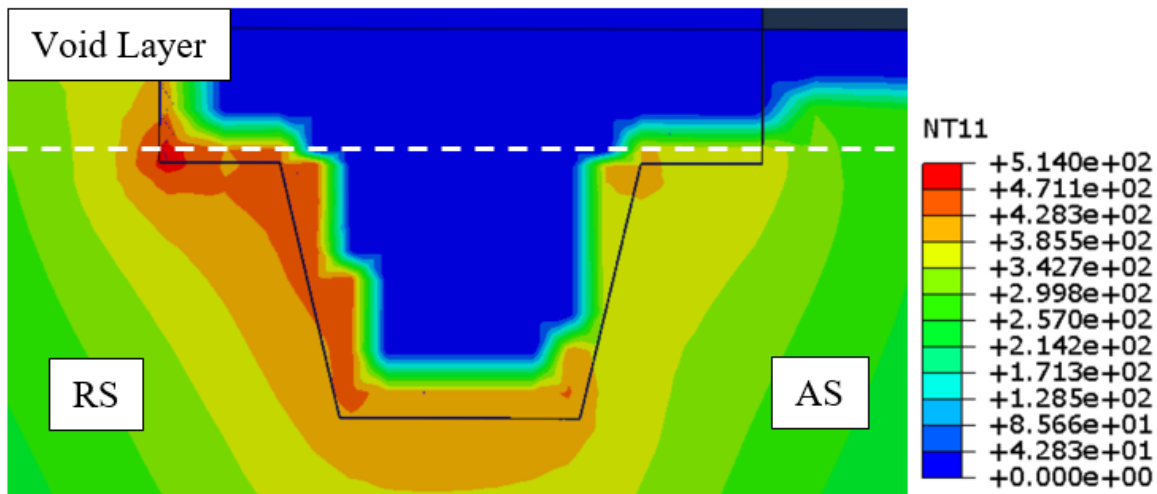


Figure 4-5: Temperature distribution in the case of tunnel defect.

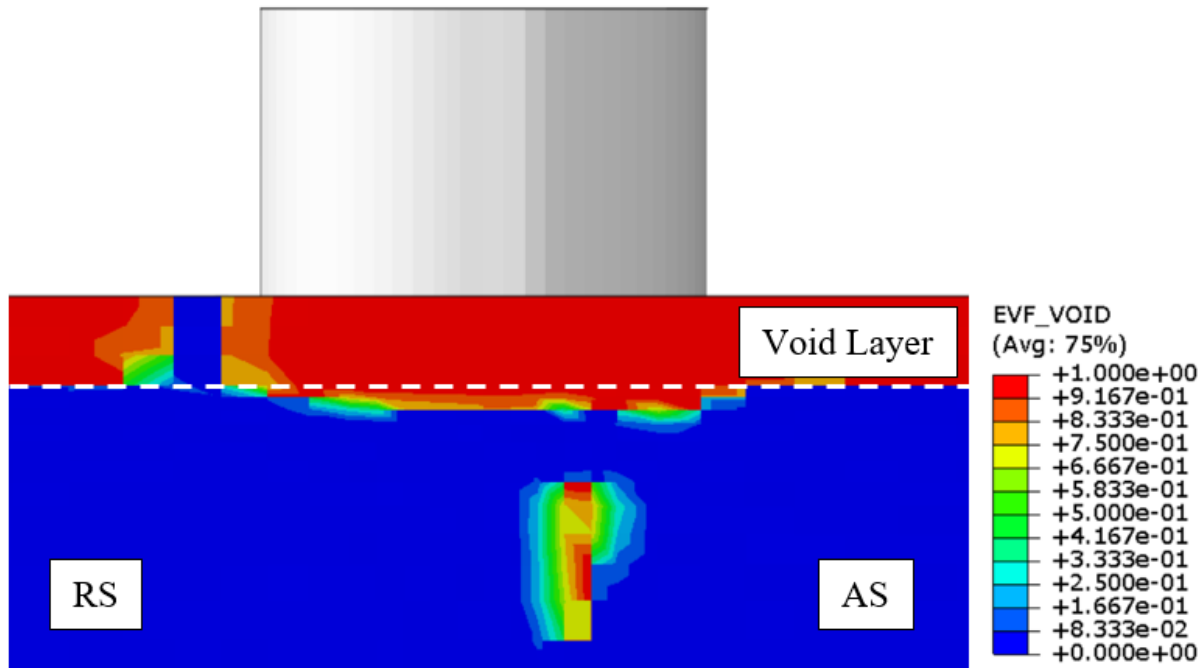


Figure 4-6: EVF_Void distribution in the case of Cavity defect. A void is noticed at the advancing side.

4.2 Friction stir additive manufacturing

4.2.1 Peak temperatures observed in the model

In precipitation hardened materials such as Al6061, the peak temperature attained during the process affects the material's properties. The finite element model is used to predict and study the peak temperatures observed during the process. Figure 4-7 shows the temperature contour at the cross-section behind the tool where the maximum temperature is expected. As can be seen from the figure, the temperature distribution is nearly symmetric in the stir zone, but higher peak temperatures are observed on AS side (Figure 4-8), while the propagation of heat in the sample is higher on the retreating side.

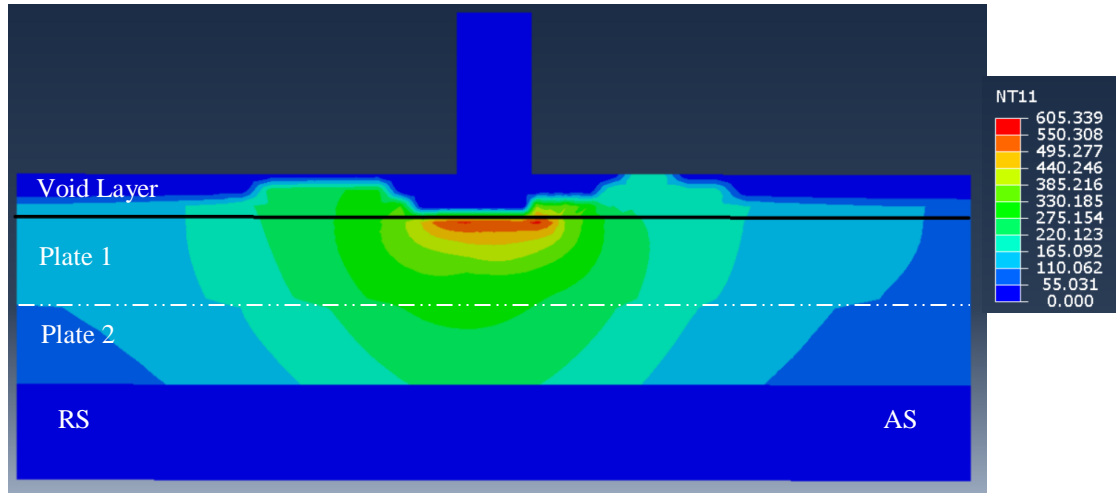


Figure 4-7: Temperature contour at the cross-section.

Figure 4-8 shows the plots of peak temperature at the cross-section in the top and bottom plate. The temperatures are measured at a distance of 0.75 mm and 1.75 mm from the top surface. It can be noted that the temperatures in the bottom plate is lower than that of the top plate, which is expected due to the fact that heat is generated in the top plate due to friction by the shoulder of the tool. The main source of heat in the FSAM processes is the heat due to friction from the tool shoulder and plastic deformation. In the bottom plate, the source of heat is the heat generated by the rotating tool tip and also the heat transferred from the top plate. Since the two plates are in contact by the fastening of bolts, and the plates are not perfectly flat, there will be some thermal resistance between the plates. As explained in the previous section, the FE model was designed to account for this thermal resistance by introducing a thermal insulating layer between the two plates. Figure 4-8 shows that higher temperatures are observed further outside the stir zone in the upper plate as compared to the bottom plate. This means that the heat affected zone in the upper plate is larger than that in the bottom plate. Figure 4-9 shows the peak temperature plot at the center of the weld along the depth of the plate, where the peak temperature of 500 °C is reached at the surface of the plate. As one goes down in the plate, the temperature drops to around 275 °C just outside the stir zone. As expected, high temperatures are observed in the top plate influenced by the shoulder effect than in the bottom plate.

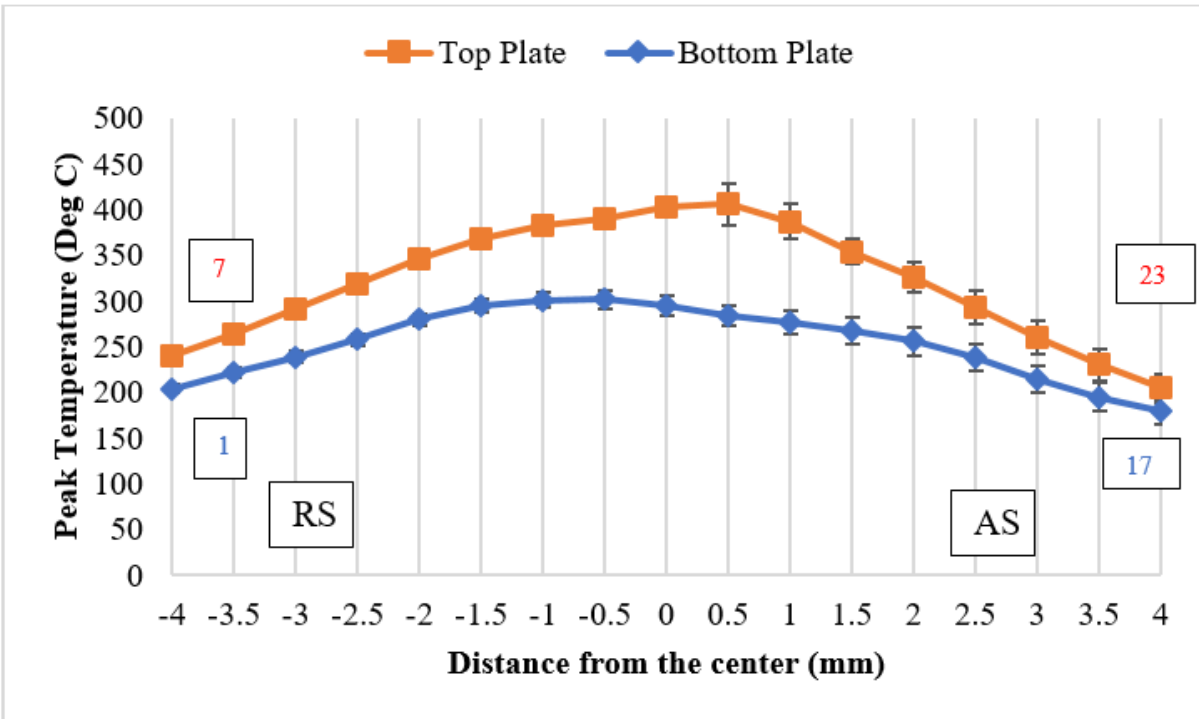


Figure 4-8: Peak temperature plot horizontally. Data points numbered correspond to the location on Figure 4-14.

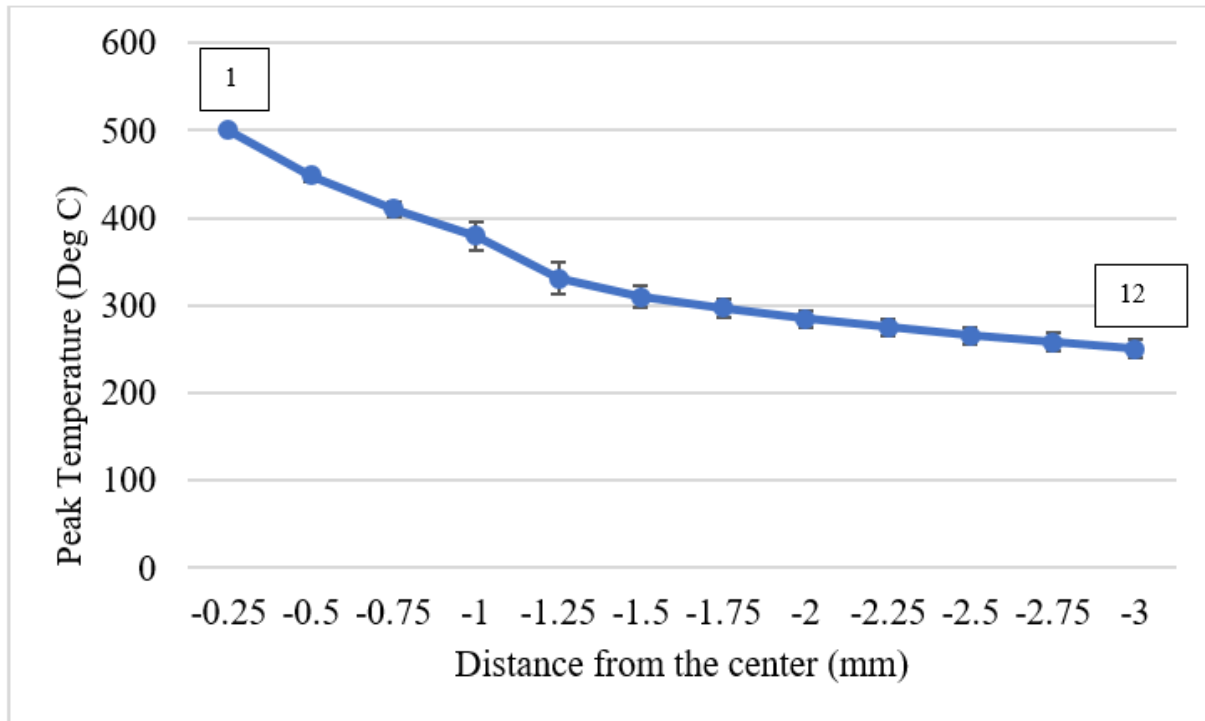


Figure 4-9: Peak temperature plot in the vertical direction. Data points numbered correspond to the location on Figure 4-14.

4.2.2 Microstructure observation

The cross-section of a friction stir weld sample is characterized by four welding zones: namely, stir zone (SZ), which is the weld zone, thermo-mechanically affected zone (TMAZ), heat affected zone (HAZ), and base metal (BM), as shown in Figure 4-10. The SZ is the zone where the tool stirs the material, also known as weld nugget. The TMAZ is exclusive to friction stir processes and is located in the vicinity of the stir zone. The HAZ is found outside TMAZ on either side. The transition from TMAZ to SZ is sharp on the advancing side and more gradual on the retreating side. As a result, there appears to be a well-defined boundary on the advancing side (AS) between TMAZ and SZ. The microstructure was observed under an optical microscope and a scanning electron microscope (SEM). To calculate the grain size, FIJI ImageJ software was used as well as the line-intercept method. Figure 4-10 also shows the locations of the optical micrographs presented in Figure 4-11.

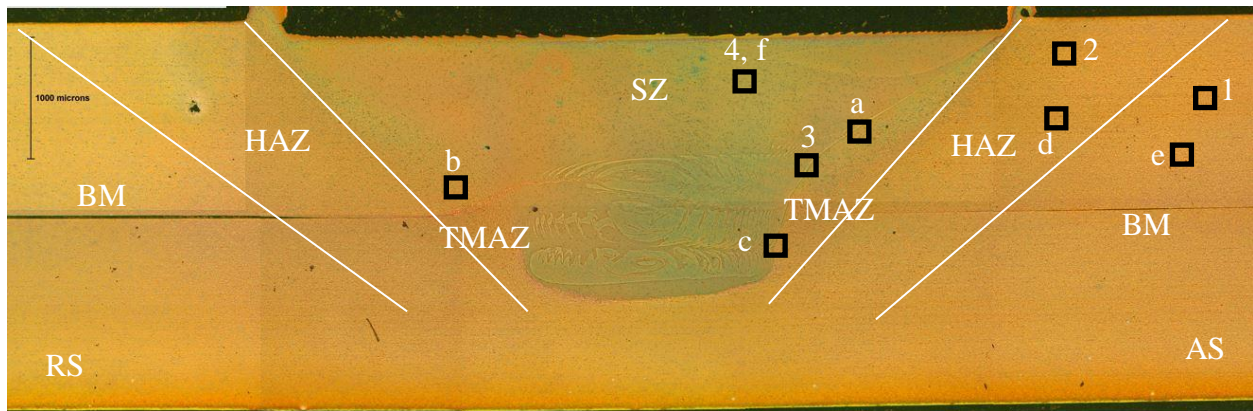


Figure 4-10: Macrostructure after Weck's etching with the various zones and location for the images

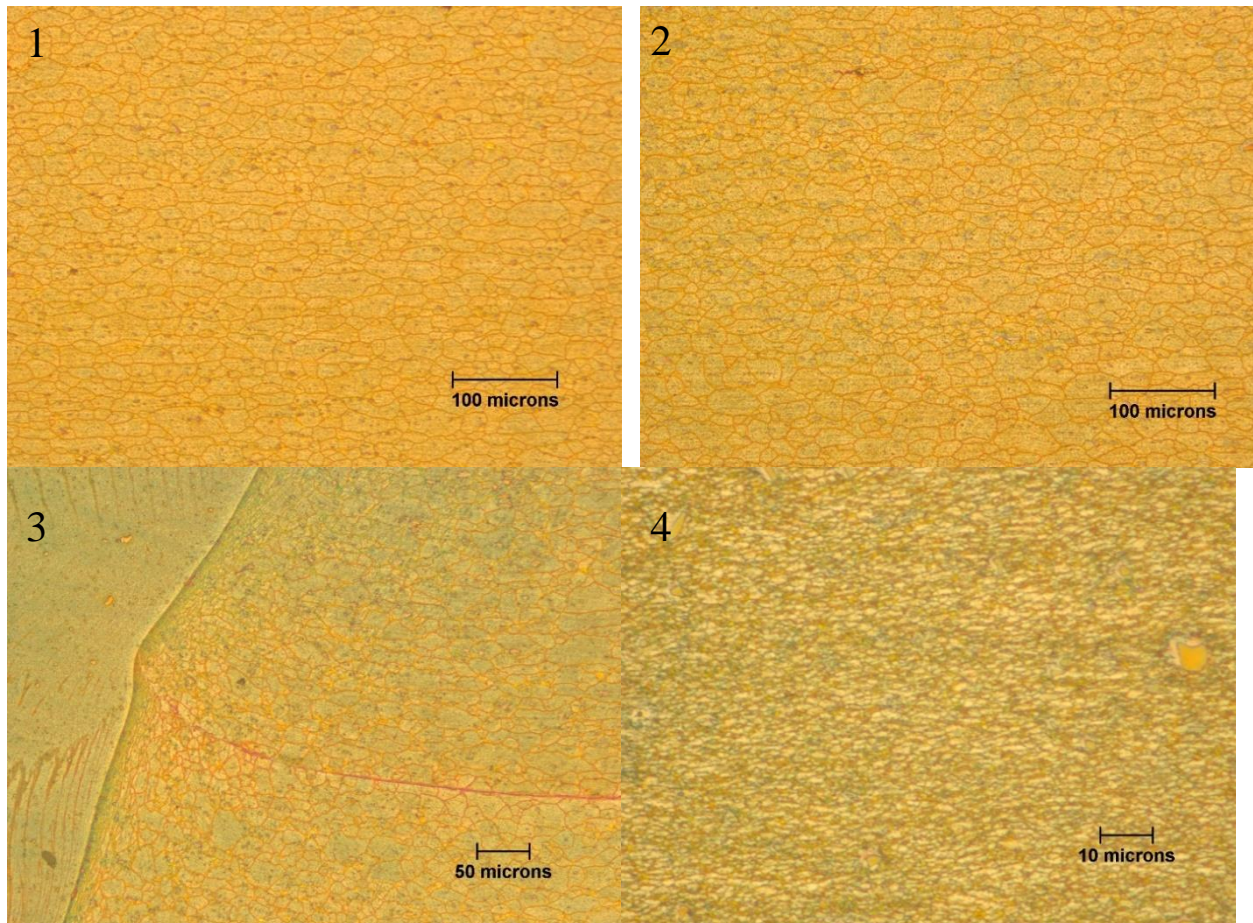


Figure 4-11: Optical Micrographs of Base metal (Location 1), Heat Affected Zone (Location 2), Thermo-mechanically affected zone (Location 3), and Stir zone (Location 4).

In the SZ, due to high plastic strain and relatively high temperatures, the material undergoes dynamic recrystallization. As a result, very fine equiaxed grain structure is observed. The optical micrograph of the SZ is shown in Figure 4-12(f). This zone is roughly the size and shape of the tool pin used. A notable characteristic of this zone includes the bands observed at the bottom, which are called ‘Onion Rings’ since they resemble an un-peeled onion. The bands are formed by the motion of the tool, with the distance between them dependent on the tool’s rotational and translational speed. FIJI ImageJ was used to calculate the grain size, which was found to be $1.55 \pm 0.54 \mu\text{m}$. Even with such small grains, lower hardness was observed in this region. The high temperatures in this zone, as predicted by the FE model, especially in the top plate, lead to the dissolution of β'' and β' precipitates and the drop in hardness. However, further down the zone, as the peak temperature decreases, the hardness increases.

The TMAZ is the transition between the SZ and the HAZ, which undergoes both the temperature change and plastic deformation. The grain size observed in the TMAZ was $9.32 \pm 6.37 \mu\text{m}$. The grains adjacent to the SZ are plastically deformed and are columnar in shape. Here, the grains are considerably deformed without undergoing recrystallization. In the bottom plate, the hardness measured was slightly lower in this zone as compared to the SZ. This is owing to the dissolution of the precipitates and having a large grain size. Figure 4-12 (a, b, c) shows the SEM micrographs in the vicinity of the stir zone. Locations a and c are on the AS side, and location b is on the RS side. The narrow and long grains were observed to be pointing in the direction of tool movement, upward on the AS and downward on the RS, as shown in Figure 4-12 (a, b, c).

The HAZ is affected only by the thermal cycle of the process and not the plastic deformation. The grains observed were around $13.32 \pm 7.77 \mu\text{m}$, which is slightly smaller in size, but the same in shape as compared to that of the base metal. Figure 4-12 (d) shows the microstructure of the HAZ on the AS side. It contains a mix of smaller and larger size grains. The hardness overserved here is lower than that of the base metal, around 90 HV. The drop in hardness compared to the base metal is explained by the thermal changes observed in this zone. This zone contains β' precipitates as the peak temperature is lower than TMAZ and SZ, thus resulting in higher hardness compared to the other two zones, but lower hardness compared to the base metal, which does not undergo much thermal change and contains β'' precipitates. The

extent of this zone is larger in the upper plate as compared to the lower plate, owing to the more heat generated at the top by the shoulder as opposed to the tool pin at the bottom.

The microstructure of the base metal is characterized by irregular shaped and pancake-shaped grains. Figure 4-12 (e) shows the microstructure of the base metal on the AS side, as observed from an SEM. The silver particles are iron-rich phases or intermetallic particles [70]. The average grain size was found to be $16.53 \pm 7.05 \mu\text{m}$, and the size of the grains is irregular. The base metal, which was T6 aging treated, has undergone very little thermal effects and so it contains β'' needle shape precipitates, which are the source of its strength. The hardness of 110 HV is found here.

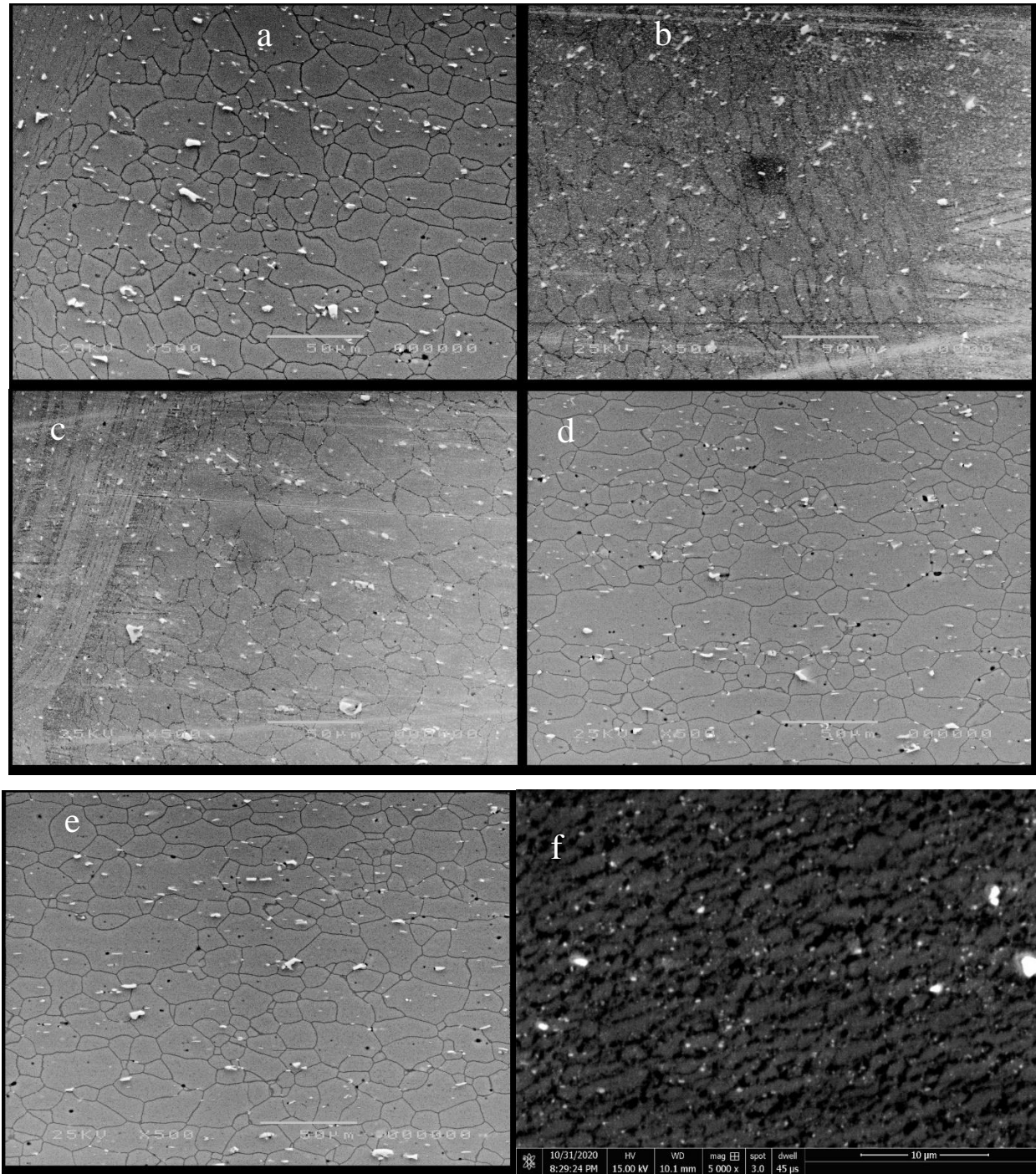


Figure 4-12: SEM Micrograph of the TMAZ around the tool at locations a, b and c; SEM Micrograph of the HAZ at location 'd'; SEM Micrograph of the Base metal at location 'e'; SEM Micrograph of the Stir zone at location 'f' from Figure 4-10.

The grain size distributions among the different zone are shown as a histogram in Figure 4-13. The base metal consists of a wide range of grain sizes, with the maximum in the range of

10-15 microns. The maximum size observed was 40 microns. The grains were irregular in shape in the rolling direction. In the heat affected zone, the grain size was irregular, with the maximum number of grains being in the range of 5-10 microns. The reduction in the size of grains is observed from BM to HAZ. Finer grains were observed in the TMAZ as it underwent plastic deformation. The grains in the vicinity of the stir zone were smaller in size (around 5-6 microns). The stir zone consisted of very fine grains equiaxed grains with an average grain size of 1.55 microns.

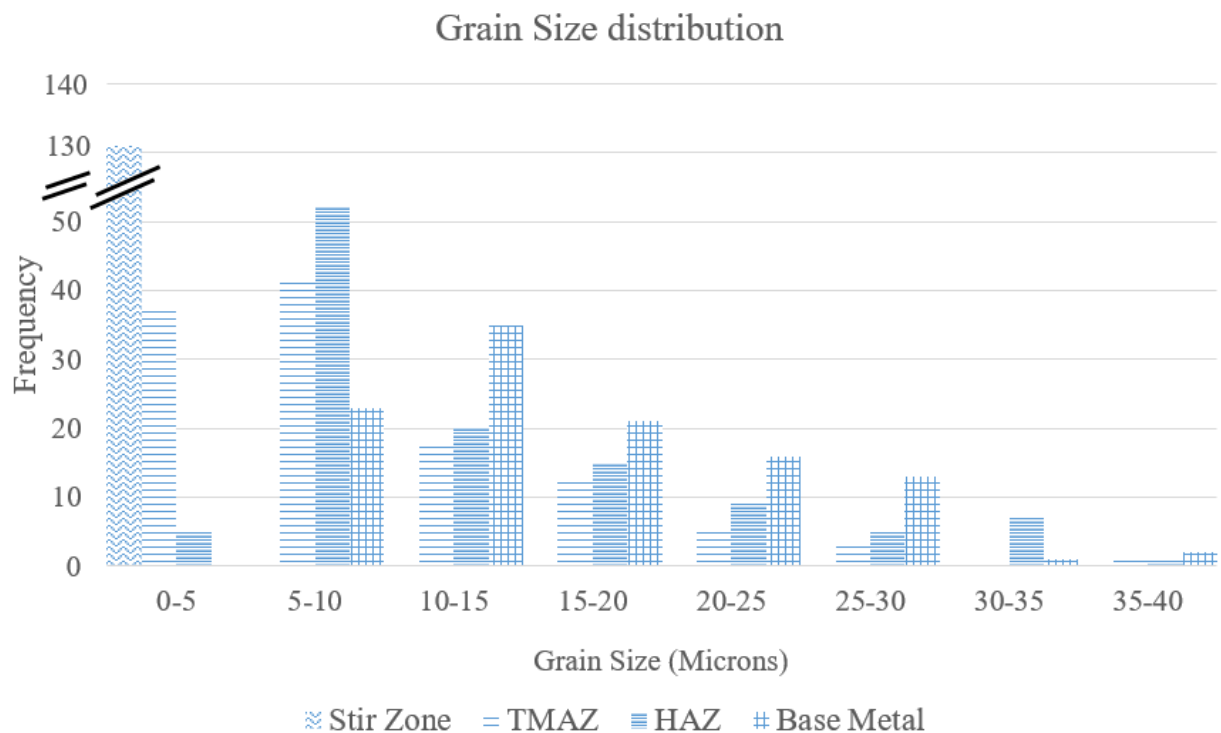


Figure 4-13: Histogram showing the grain size distribution in the different zones.

4.2.3 Microhardness analysis

Material behavior

The mechanical properties of Al6061 are controlled by the precipitates in the material. The as-received material of Al6061-T6 is known to contain β'' precipitates, which are the main source of its strength. During the FSAM process, high temperatures are reached, which affect the

microstructure and the material properties. The precipitation sequence in Al6061 is described as follows [71]:

SSSS \rightarrow solute clusters \rightarrow GP zones spherical \rightarrow β'' (needle) \rightarrow β' (rod) \rightarrow β ,

where β is the equilibrium phase Mg_2Si .

As mentioned before, the β'' phase is the main factor for the strengthening of Al6061-T6 alloys, which are needle shaped [72]. These needle-shaped precipitates are very thin and are densely populated. They lead to increased hardness by hindering the dislocation movement. When the material is heated to around 240 °C, the semi-coherent β'' precipitates acquire a more stable β' phase due to increased atomic diffusion. In the β' phase, the precipitates are larger in size and are rod-shaped [73]. These precipitates now have a lesser contribution to strengthening. If the heating further continues, the precipitates turn into a fully distinct β phase, which has no coherency with the base structure. β' precipitates dissolve around 360-380 °C and form the β phase, which consists of platelets shaped precipitates. This phase is unable to arrest the motion of the dislocations but can only cause hindrance. Hence, the material loses its strength as it is heated to higher temperatures owing to the loss of precipitates. The relation between temperature and phases is shown in Table 4-1.

Table 4-1: Temperature ranges for different phases.

Temperature range	Phase
~160-240 °C	β''
~240-380 °C	β'
~380-480 °C	β

Observation and comparison

The mechanical properties of the joint are analyzed by the measurement of microhardness along with the predictive modeling that elucidates the resultant hardness variation. Hardness profiles give a clear picture of the thermo-mechanical conditions that the material went through during friction stir welding. In this study, transverse hardness was measured in both the top and bottom plates. To monitor the changes along the depth, hardness in the vertical direction in the middle of the stir zone was also measured, as shown in Figure 4-14. The hardness was measured

at a distance of 0.75 mm and 1.75 mm from the top surface: The first measurement is in the top plate, and the second one is in the bottom plate. The transverse hardness was measured at an interval of 0.5 mm, and the vertical hardness was measured at an interval of 0.25 mm.

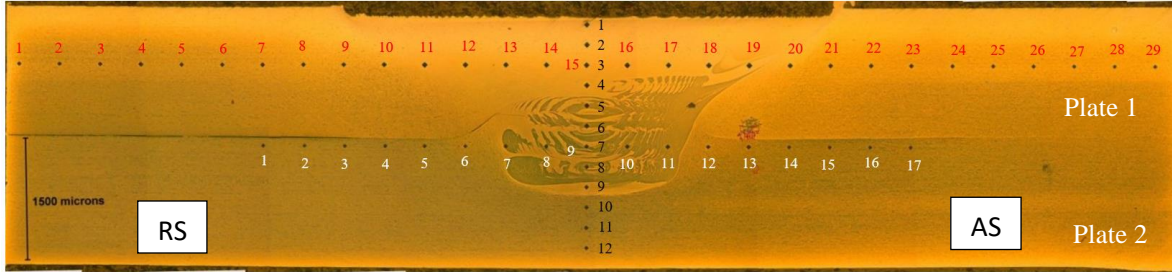


Figure 4-14: Measured hardness map

The hardness of the material is predicted with the help of the finite element model and an empirical relation. The temperature data predicted by the FE model is used to predict the hardness of the material using a relation between hardness, temperature, and natural aging time proposed by Esmaeili et al. [74]:

$$HV = A_T + B_T \times \ln t,$$

where $A_T = 3.7 + 25600 \times 1/T$, and $B_T = \exp(63 \exp(-1600/T) - 2)$, T is the peak temperature reached in $^{\circ}\text{C}$ and t is the natural aging time in seconds. The term A_T is the hardness right after welding, and the term B_T represents the aging kinetics. The time used in this study was 10^5 seconds, as the measurements were conducted after one day. The model is not valid for temperatures below 220°C and above 565°C . This model has been employed by Mrowka-Nowotnik et al. [75] to study Al6005 and Al6082, and by Woo et al. [76] to predict hardness in Al6061 after FSW.

As can be seen in Figure 4-15 and Figure 4-16, the hardness is lower within the stirred zone in both the top and bottom plates. This is owing to the dissolution of the precipitates, as mentioned earlier. Lower hardness is also observed in the top plate as compared to the bottom plate. In the top plate, high temperatures are achieved, as seen in Figure 4-8 and Figure 4-9. With temperatures higher than 360°C in the top plate in the stir zone, the β phase is found in the zone, which explains the considerable amount of drop in the hardness to around 65 HV. Slight variation in hardness was observed in the thermo-mechanically affected zone (TMAZ) compared to the other regions, as seen in the error bars in Figure 4-15. In the upper plate, similar low

hardness was observed in both SZ and TMAZ. Base hardness was measured at a distance of 6.5 mm from the center at data points 2 and 28.

In the bottom plate, lower temperatures are observed as explained above, around 280 °C – 300 °C in the stir zone. Lower temperatures lead to the β' phase, where the precipitates are rod shaped and are larger in size. The presence of this phase leads to higher hardness, as observed in the stir zone, around 78 HV. The lowest hardness was observed in the TMAZ zone. Base material hardness was measured at a distance of 3.5 mm from the center at data points 2 and 16. While going down the thickness of the plate, the temperature decreased as shown in Figure 4-9, and the hardness was found to increase as shown in Figure 4-17, nearly approaching the base hardness of 110 HV of Al6061-T6 at a distance of 3 mm from the top at data point 12.

The FSAM process leads to recrystallization and formation of a very refined equiaxed grain structure in the stir zone. According to the Hall-Petch relation, a finer grain size should lead to increased hardness of the material. However, as discussed previously, Al6061 is a precipitation-hardened material, and it derives its strength primarily from the precipitates. The reason for the drop in hardness in the stir zone is due to the loss of precipitations.

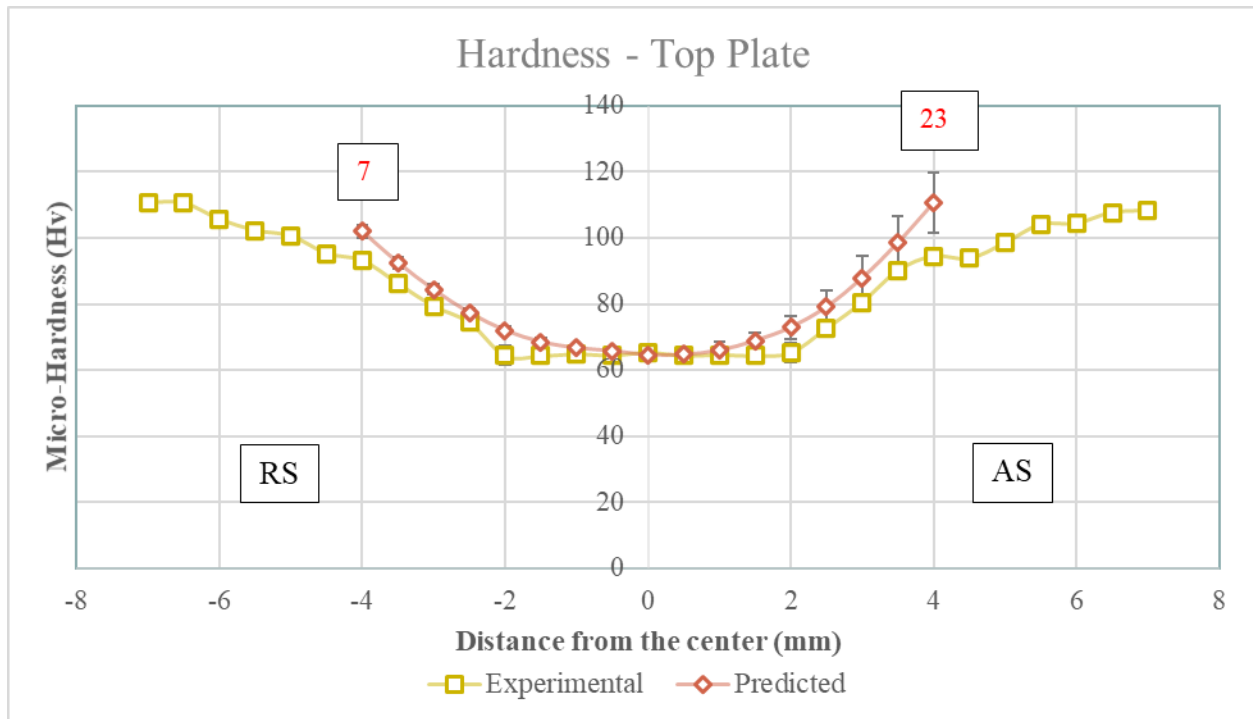


Figure 4-15: Comparison of hardness in the top plate. The numbered data points correspond to the hardness map in Figure 4-14.

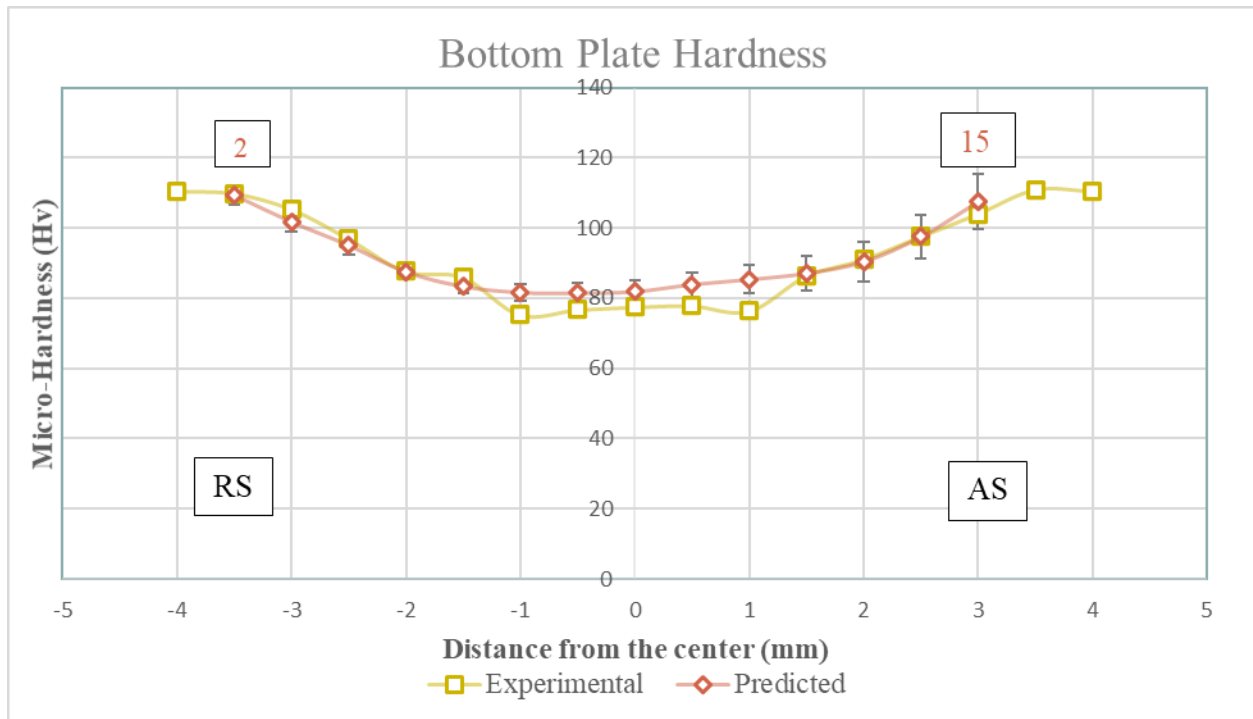


Figure 4-16: Comparison of hardness in the bottom plate. The numbered data points correspond to the hardness map in Figure 4-14.

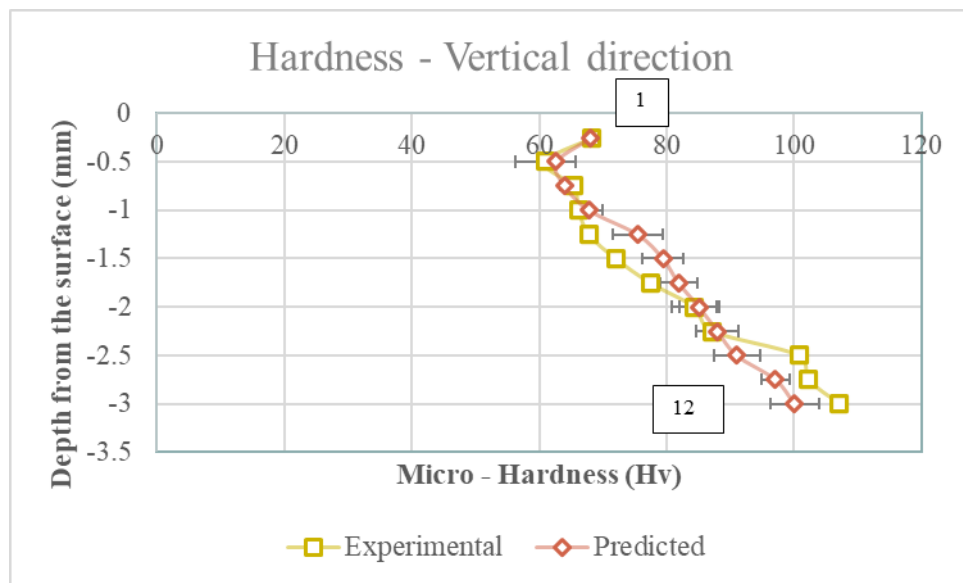


Figure 4-17: Comparison of hardness in the vertical direction. The numbered data points correspond to the hardness map in Figure 4-14.

4.2.4 Analysis of mechanical properties

Tensile test

To test the mechanical properties of the additive manufactured Al6061, a tensile test was conducted. Two 1.6 mm plates were added on top of each other for the purpose of the test. The dimensions of the tensile test specimen are shown in Figure 4-18 as per ASTM standard B557M for a subsize specimen [65]. The sample was made by making multiple passes in the Y – direction, as shown in Figure 4-19. The tensile specimen was cut out in the Y – direction. The thickness of the material was not sufficient to be tested in the build direction (Z-direction); therefore, a tensile shear test was conducted to test the bonding strength.

Three samples were tested, and the results were averaged. The ultimate tensile strength (UTS) and yield strength of the FSAM processed sample was 227.52 ± 10.42 MPa and 190.06 ± 1.97 MPa, respectively. These strength values for the as-received samples were 317.61 ± 1.17 MPa and 252.11 ± 1.97 MPa, respectively. A reduction of 28.36 % and 24.61 % in UTS and yield strength was observed from FSAM samples as compared with the as-received ones. A significant reduction in the percentage elongation of 59.55% was observed: from 15 ± 1.87 % in the as-received sample to 6.06 ± 2.08 % in the FSAM processed sample. The mode of failure was necking and the fracture at the TMAZ of one of the passes. The hatch distance (distance between two consecutive tool passes) in these samples was 4 mm. Samples with a lower hatch distance of 2 mm were also tested. The strength values were reduced slightly with yield strength and UTS being 226.03 ± 11.43 MPa and 174.89 ± 12.07 MPa respectively. This could be attributed to the high process temperature reached due to the increase in the number of tool passes. However, the percentage elongation is improved to 6.83 ± 0.85 %. Figure 4-20 shows the true stress vs. strain curves of the as-received material and the FSAM processed sample (hatch distance of 2 mm). As can be seen from the figure, the elastic region of the two materials is nearly identical. Figure 4-21 shows the fractured specimen after test.

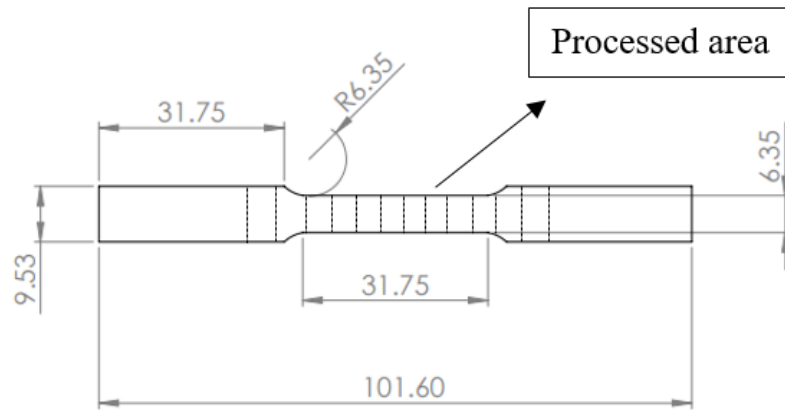


Figure 4-18: Dimensions of the Tensile test specimen (mm).

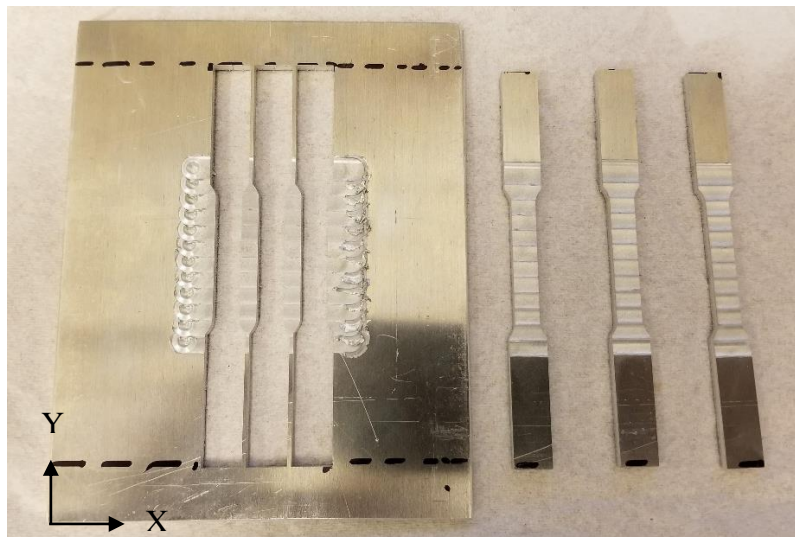


Figure 4-19: Machined tensile test samples.

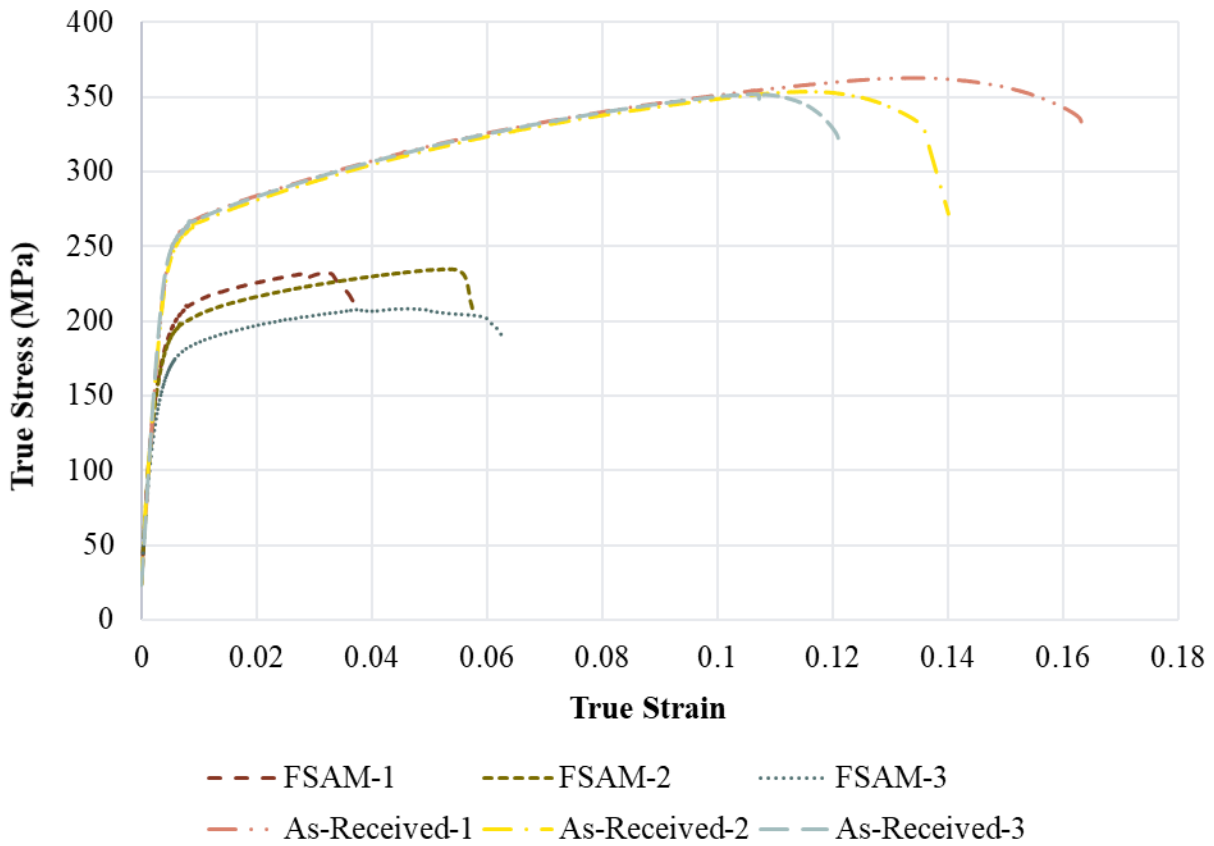


Figure 4-20: Stress vs. strain curve for the as-received and the FSAM processed sample (2 mm hatch distance).



Figure 4-21: Tested FSAM processed sample after fracture .

The strength values and percent elongation of parts produced by the FSAM process are comparable with those of Ultrasonic AM (UAM), another solid-state AM technique. However, better strength values are observed as compared to the fusion-based AM techniques like Selective Laser Melting (SLM), Direct Metal Laser Sintering (DMLS), and a heated bed Laser

Powder Bed Fusion (LPBF). Sridharan et al. [77] and Cakmak et al. [78] conducted UAM on Al6061 and reported yield strengths of around 221 MPa with percent elongation at 6 % and 5.6 %, respectively. The yield strength in FSAM is slightly lower as compared to UAM, but the percent elongation is slightly better. Sridharan et al. [77] reported the UTS to be 224 MPa, which is similar to FSAM. In the case of SLM, Maamoun et al. [79] reported the yield strength values varying from 125 MPa to 172 MPa, which are much lower than the FSAM value. Uddin et al. [80] studied heated-bed LPBF on Al6061, and reported the yield strength of 70.5 MPa, UTS of 137 MPa and 13 % elongation. Compared with LBPF processes, FSAM yielded higher yield strength and UTS but lower ductility.

Tensile shear test

In order to test the bonding strength of the two plates, a lap weld sample was fabricated. A tensile shear test was conducted to investigate the load carrying capacity of the weld as a substitute for conducting testing in the build direction. A single weld pass was made to join the two plates so that the strength of the weld could be tested. The dimensions of the specimen are shown in Figure 4-22. The lap weld samples are shown in Figure 4-23.

For lap weld study, the weld joint efficiency is calculated by using the maximum load capacity of the sample. The joint efficiency is given by the formula [81]:

$$\text{Joint Efficiency} = \frac{\text{Maximum load capacity of the joint}}{\text{Cross-section area of the sample} \times \text{Tensile strength}} \times 100$$

This formulation does not consider the area of the weld, but just the cross-section area of the sample. However, it tells you how much closer the weld strength is to the parent metal's tensile strength.

Table 4-2 presents the load at failure and joint efficiency measured of the three samples tested. The average load was observed to be 5915.9 ± 53.54 N, and the average joint efficiency was calculated to be 48.35 ± 1.78 %. The fracture at all three samples was close to the TMAZ on the retreating side. The hardness measured was among the lowest at that point in the top plate, around 66 HV, and the lowest in the bottom plate, around 75 HV, as can be seen in Figure 4-15 and Figure 4-16. Also, the hooking defect is observed at the TMAZ on the retreating side, which

leads to the reduction in effective plate thickness, which could be the reason why the fracture occurred at TMAZ of the top plate. Figure 4-24 shows the specimen after testing and the fracture, and Figure 4-25 shows the weld cross-section with the fracture region. A higher magnification image of the defect between the two plates is shown in Figure 4-26.

The average failure strength of the specimen was calculated to be 144.31 ± 1.65 MPa. Fadaeifard et al. [82] reported the failure strength values for Al6061. In their study, they reported the shear strength to vary from 138 MPa to 95 MPa by varying RPM from 900 to 1200. They found this to be dependent on tool RPM and concluded that the shear strength decreases with increasing RPM. For an operating tool rotational speed of 1800 RPM, in this study, a higher failure strength is observed.

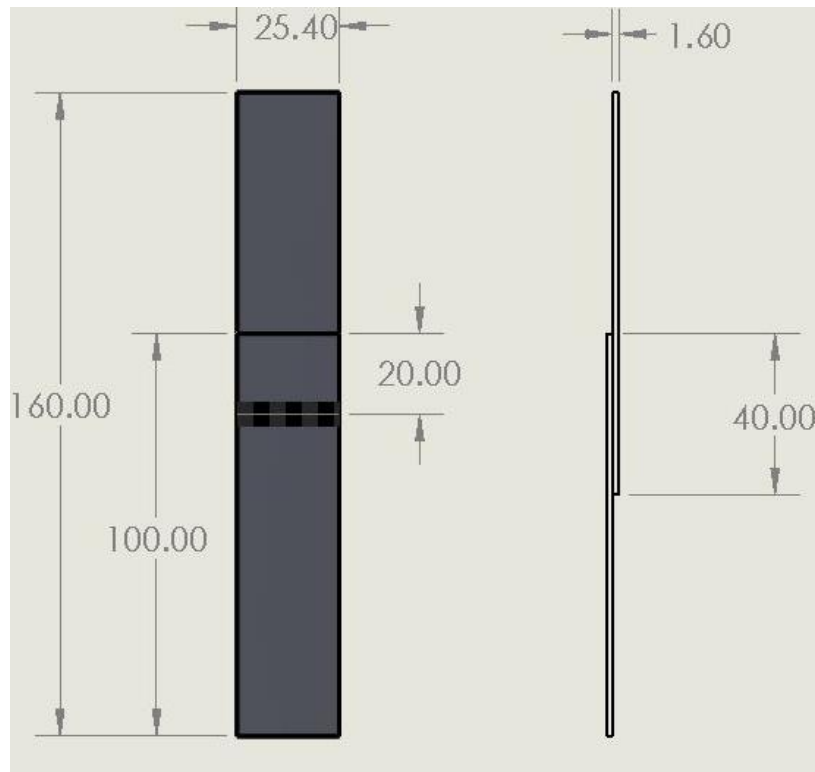


Figure 4-22: Dimensions of tensile shear test specimen (mm).



Figure 4-23: Friction Stir lap weld sample and Tensile shear test specimen..

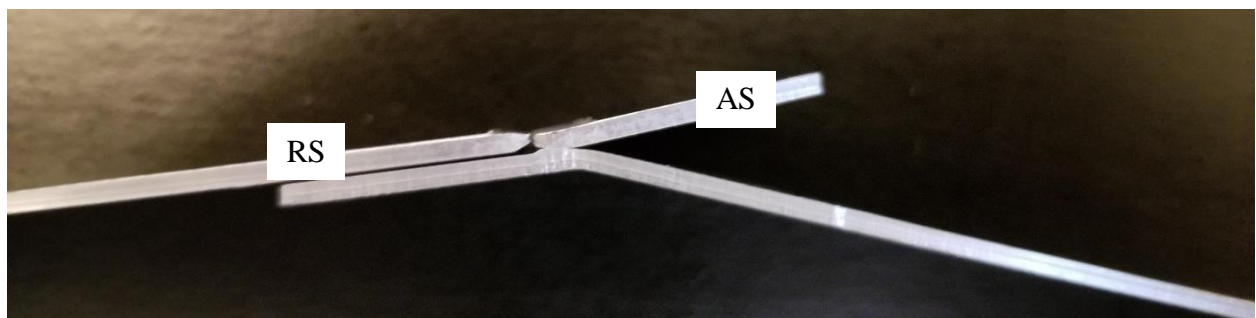


Figure 4-24: Tested lap weld sample.

Table 4-2: Tensile shear test results with the calculated joint efficiency.

	Load at Failure (N)	Joint Efficiency (%)
Sample 1	5969.51	49.99
Sample 2	5942.82	49.20
Sample 3	5844.97	45.87

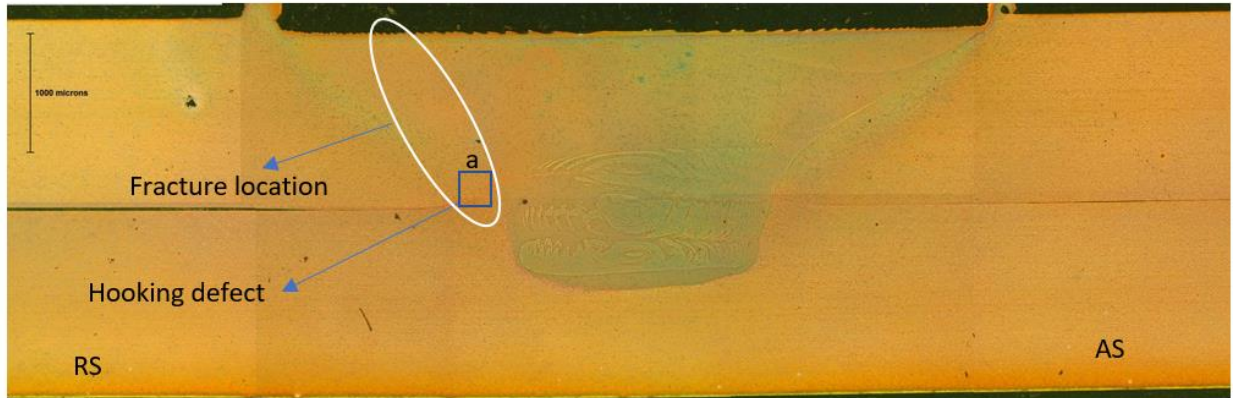


Figure 4-25: Weld cross-section with the fracture location.

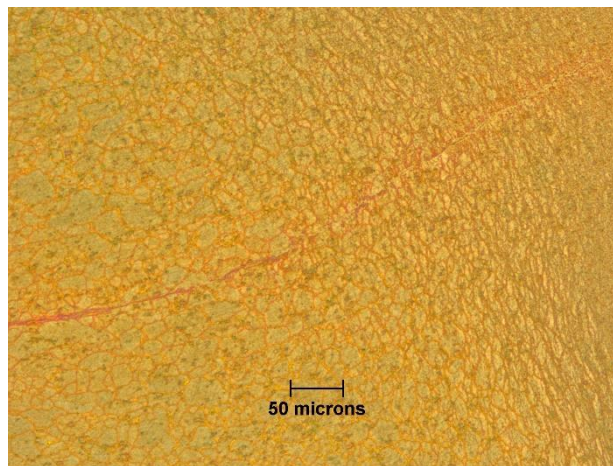


Figure 4-26: Close-up image of the hooking defect at location 'a' in Figure 4-25.

4.2.5 Defects observed

Friction stir additive manufacturing involves adding plates on top of each other, which in principle is similar to lap welding. Defects in lap welding include the volumetric defects which are observed in butt welding, as studied in this thesis, but also observe other types of defects such as, hooking defect, kissing bond defect and plate thinning [83]. Hooking defect is observed

on the advancing side as well as the retreating side at the interface between the two plates in the thermo-mechanically affected zone (TMAZ). It appears as the interface is pulled up in the top plate. It is found that increasing the welding speed and decreasing the tool rotational speed helps in reducing this defect [84]. Kissing bond defect is visible on the retreating side of the stir zone. Kissing bond occurs due to the sub optimal stirring at the interface between the two plates with the remains of oxide layer [85, 86]. The upper plate thinning is a result of both these defects.

In this study, the top plate of 1 mm and 1.6 mm thicknesses were studied. Figure 4-27 and Figure 4-28 show the weld macrostructure of both the configurations, with the hooking and kissing defects visible. In the two configurations studied in this study, the width of hooking defect was found to be similar in both the samples, around 0.14 mm as can be seen in Figure 4-27 and Figure 4-28. The major difference was observed in the width of the kissing bond defect in the stir zone. In the first sample (1 mm thick top plate), the width was throughout the length of the stir zone, resulting in thinning of the upper plate. Figure 4-29 shows the interface along the length of the stir zone. In the second sample (1.6 mm top plate), the width was considerably less around 1.25 mm as shown in Figure 4-30, ensuring effective mixing in the stir zone and reducing the thinning of the upper plate. Figure 4-30 also shows the close-up of the hooking effect of the tool.

Figure 4-31 shows the addition of one 1 mm plate onto the substrate. Figure 4-32 shows the cross-section of the two 1 mm thick plates added on the substrate. Five different passes were made to add a rectangle of plate on the substrate. It was seen that after adding the second plate, voids were observed at the bottom of the tool, as highlighted in Figure 4-32. Since the addition of first plate shown in Figure 4-31 does not contain any volumetric defects, the reason for those defects while adding the second plate could be attributed to a gap that present between the first and second plates. A gap exists because of the plunge depth of the previous plate. This gap can be filled by increasing the plunge depth which would increase the forging pressure and the fill that void. In addition to that, use of a force control machine other than a position control machine can help alleviate this defect.

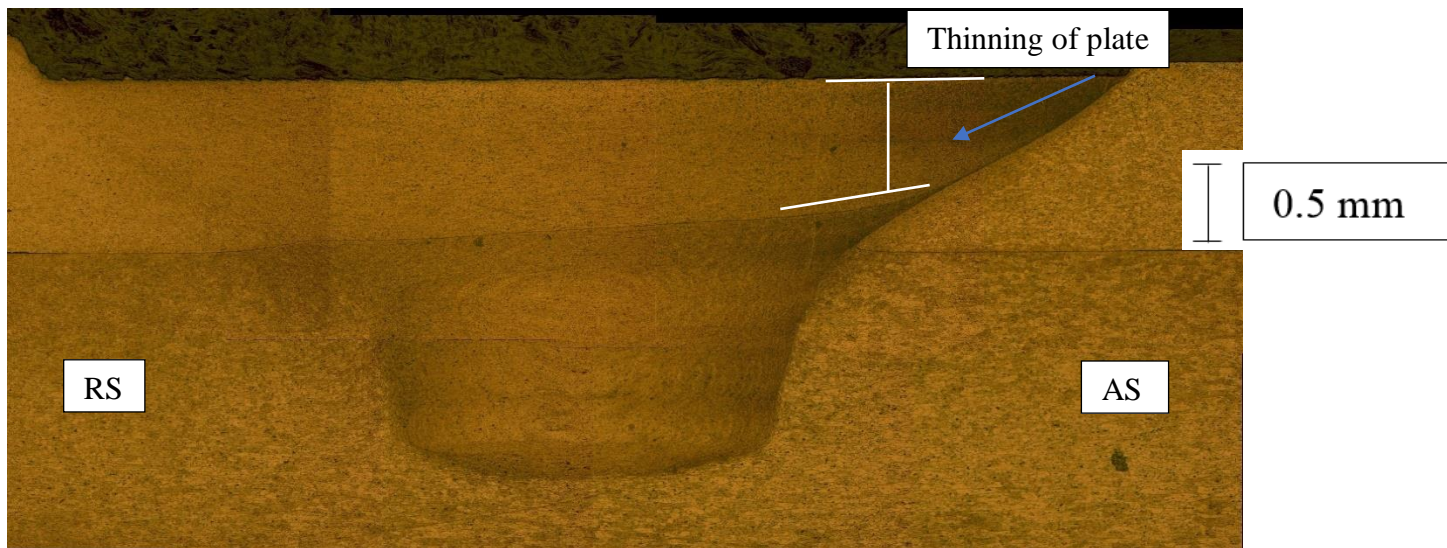


Figure 4-27: Weld macrostructure of 1 mm + 3.17 mm plates.

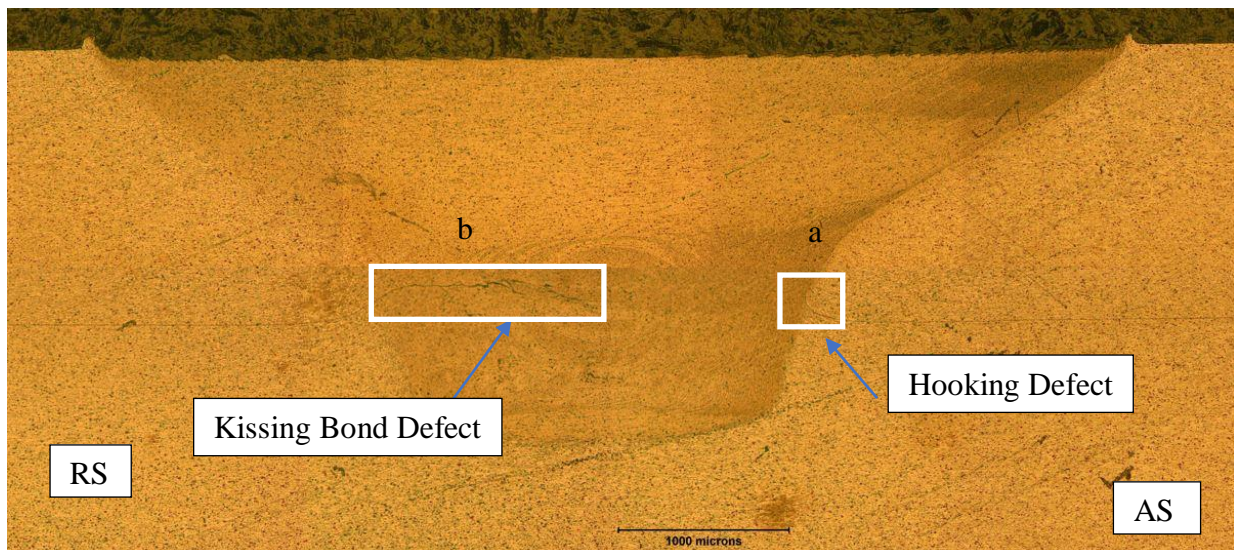


Figure 4-28: Weld macrostructure of 1.6 mm + 1.6 mm plates.

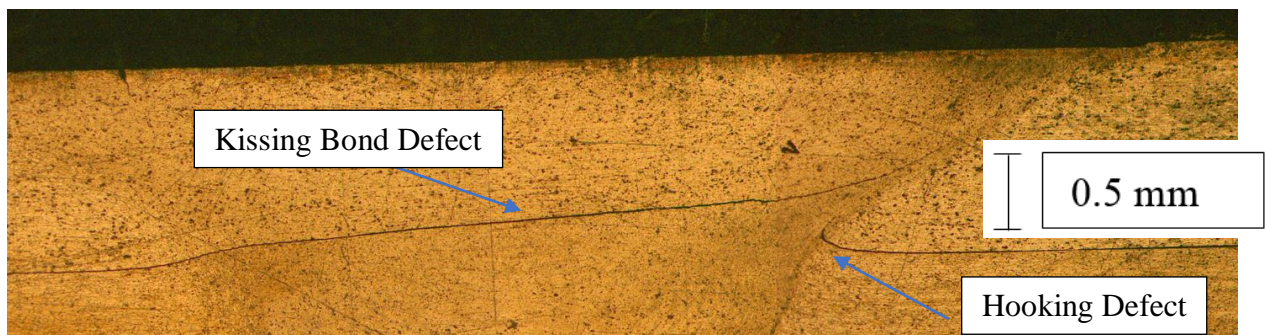


Figure 4-29: Close-up of defects from Figure 4-27.

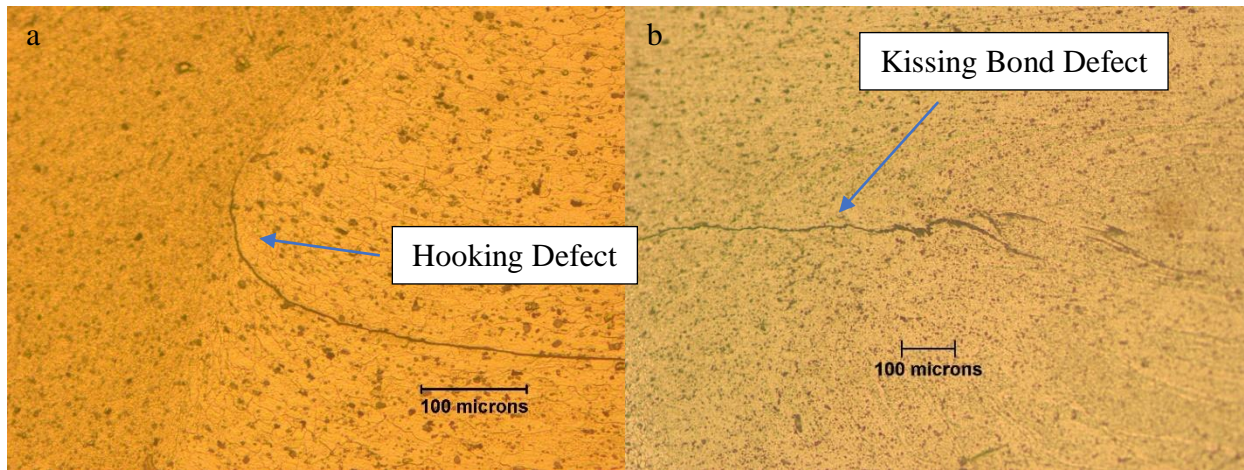


Figure 4-30: Close-up images of hooking and kissing bond defect from Figure 4-28.



Figure 4-31: Macrostructure of the addition of 1 mm plate to a 3.17 mm plate.

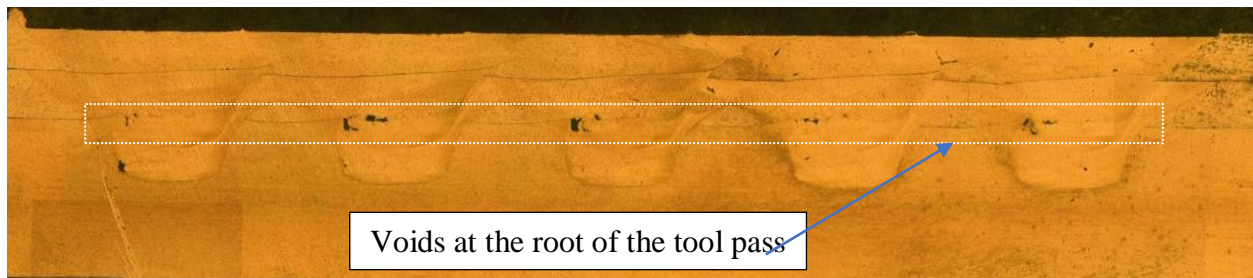


Figure 4-32: Macrostructure of addition of two 1 mm plates on a 3.17 mm substrate.

5. CONCLUSIONS

5.1 Conclusions

A CEL FE model was developed to successfully predict the process parameters and the axial forces on the tool for FSW and FSAM processes. The model was validated via experiments. For welding 3.17 mm thick Al6061-T6 plates, sound weld case observed at tool rotational speed of 2000 RPM and welding speed of 200 mm/min. Tunnel defects were observed at lower tool rotational speeds at tool rotational speed of 1200 RPM and welding speed of 300 mm/min. Cavity defects were observed at higher welding speeds at tool rotational speed of 2000 RPM and welding speed of 400 mm/min. Tunnel defects were a result of insufficient heat input, and cavity defects were a result of abnormal stirring. Both defects were observed on the advancing side.

A Solid-state AM technique, Friction stir additive manufacturing, was successfully performed and demonstrated on Al6061-T6. The process parameters used were tool rotational speed of 1800 RPM and welding speed of 125 mm/min, with the plunge depth as 0.11 mm. An 8 mm thick, 8 mm wide, and 40 mm long sample was fabricated by adding five 1.6 mm thick plates. The grain size observed from the microstructure images in SZ, TMAZ, HAZ, and BM was $1.55 \pm 0.54 \mu\text{m}$, $9.32 \pm 6.37 \mu\text{m}$, $13.32 \pm 7.77 \mu\text{m}$, and 16.53 ± 7.05 , respectively. An empirical relation using the temperatures predicted by the FE model is used to successfully predict the microhardness distribution in the sample. In the top plate, the hardness of 65 HV was observed in the stir zone, owing to the presence of the β phase. In the bottom plate, a higher hardness of around 78 HV was observed in the stir zone owing to lower temperatures and the presence of β' phase.

The ultimate tensile strength (UTS) and yield strength of the FSAM processed sample (hatch distance 4 mm) were $227.52 \pm 10.42 \text{ MPa}$ and $190.06 \pm 1.97 \text{ MPa}$, respectively. A reduction of 28.36 % and 24.61 % in UTS and yield strength was observed between FSAM and as-received samples. The elongation was $6.06 \pm 2.08 \%$. For the samples with the hatch distance of 2 mm, yield strength and UTS were $226.03 \pm 11.43 \text{ MPa}$ and $174.89 \pm 12.07 \text{ MPa}$, respectively, with the elongation being $6.83 \pm 0.85 \%$. A tensile shear test conducted to test the bonding strength between two plates revealed the average failure strength of $144.31 \pm 1.65 \text{ MPa}$ with $48.35 \pm 1.78 \%$ joint efficiency. The length of the kissing bond defect was observed to be

longer in case of a thinner upper plate (1 mm) as opposed to a thicker upper plate (1.6 mm) relative to the tool tip length (2.1 mm). Volumetric defects were observed while adding a second plate on top of the first one. This was a result of the gap present between the two plates. It could be dealt by increasing the plunge depth of the tool to provide more forging pressure.

5.2 Future work and applications

The FE model developed in this study can predict the sound weld parameters in terms of tool geometry, workpiece geometry, and given material. This could prove helpful as it will prevent conducting many experiments and potentially extend the tool life, and save cost and time. By predicting tool reaction forces, it could prevent machine and tool damage. This model's application to be used for FSAM shows that this model can be modified to simulate different welding configurations like a lap weld. In addition, dissimilar material welding, which is very advantageous (as in the case of Honda [21]), can be simulated. This could be made possible by partitioning the workpiece and assigning different material properties to the different partitions. Using the model to predict process temperature history and material properties like microhardness can be very useful in predicting material behavior.

The choice of a welding tool can determine the size of the window (shown in Figure 1-2) in which sound welds can be obtained. Two main characteristics of a tool are the shoulder and the tool pin probe. The tool tip's shape and feature depend on the application, and they may vary for a butt weld and a lap weld. As mentioned previously, in FE simulations, featured tips promote better mixing of materials than featureless tips, and hence they have a greater operational window for the sound weld. Approximations of these features on the tool in an FE model can lead to an accurate prediction of the process. In this study, the tool used in the FE model was tapered with flats, which was used as an approximation for a tri-flat threaded tool used in experiments. However, the use of this model can be generalized and can be used to choose an appropriate tool and predict process parameters for a welding/AM process.

In this study, the properties of the as-welded samples were tested. The mechanical properties of the FSAM processed samples after heat treatment can also be explored. The possible heat treatment for Al6061 after FSAM includes solution heat treatment followed by artificial aging or artificially aging the material. Baghdadi et al. [87] heat-treated Al6061 after FSW using solution heat treatment followed by artificial aging and observed improved

mechanical properties compared to the as-welded samples. Elangovan et al. [88] compared different post FSW heat treatment methods for Al6061-T6 and reported that artificial aging at 160 °C for 18 hours produced the best results. Heat treating FSAM samples after AM can be explored and could improve the properties.

Al6061 is a precipitation-hardened metal, and it derives its strength from the presence of precipitates. Metals that are grain boundary strengthened, i.e., in which the grain size has quite a lot of effect on the mechanical properties, can be studied. These metals obey the Hall-Petch relation saying that finer grain structure results in better mechanical properties. Since in FSAM, we get a refined microstructure in the SZ, this process could show promising results. One example of such metal is Al5083 [56].

In FSAM, adding the second or any subsequent plate after the first one could lead to voids at the tool root. The reason for this is that the FSAM processed area is not necessarily flat with the rest of the plate owing to the offset created by the plunge depth. Hence, when the next plate is mounted, there is a gap between the two. One possible way to remedy this is by conducting FSAM using force control instead of displacement control. This way, we can ensure sufficient forging pressure to ensure effective stirring between the plates.

Since we are adding two plates on top of each other, the contact between the two plates is essential. The two factors influencing contact are the clamping force of the fixture and the surface of the plate. The clamping force can be measured using the torque wrench when screwing the bolts. The surface of the plates in contact is affected by their roughness. This can be studied along with some surface preparation methods like polishing or cleaning with acetone. The effect of these factors on the quality of the weld can be studied.

In this study, two hatch spacing (distance between two consecutive tool passes) were studied. There is a tradeoff between the hatch spacing and the mechanical properties. We know, the higher the hatch spacing, the higher the throughput. However, the effect of hatch spacing on the material quality and its properties needs to be investigated in order to optimize this process.

REFERENCES

1. Vargas, J.A., Torres, J.E., Pacheco, J.A. and Hernandez, R.J., 2013. Analysis of heat input effect on the mechanical properties of Al-6061-T6 alloy weld joints. *Materials & Design (1980-2015)*, 52, pp.556-564.
2. Moreira, P.M.G.P., De Figueiredo, M.A.V. and De Castro, P.M.S.T., 2007. Fatigue behaviour of FSW and MIG weldments for two aluminium alloys. *Theoretical and applied fracture mechanics*, 48(2), pp.169-177.
3. Liang, Y., Shen, J., Hu, S., Wang, H. and Pang, J., 2018. Effect of TIG current on microstructural and mechanical properties of 6061-T6 aluminium alloy joints by TIG–CMT hybrid welding. *Journal of Materials Processing Technology*, 255, pp.161-174.
4. Hirose, A., Kurosawa, N., Kobayashi, K.F., Todaka, H. and Yamaoka, H., 1999. Quantitative evaluation of softened regions in weld heat-affected zones of 6061-T6 aluminum alloy—characterizing of the laser beam welding process. *Metallurgical and Materials Transactions A*, 30(8), pp.2115-2120.
5. Gu, D., 2015. Laser additive manufacturing of high-performance materials. Springer.
6. Thomas, W.M., 1991. Friction Stir Butt Welding, International Patent Application No. PCT/GB92. *GB Patent Application No. 9125978.8*.
7. Mishra, R.S. and Ma, Z.Y., 2005. Friction stir welding and processing. *Materials science and engineering: R: reports*, 50(1-2), pp.1-78.
8. Threadgill, P.L., Leonard, A.J., Shercliff, H.R. and Withers, P.J., 2009. Friction stir welding of aluminium alloys. *International Materials Reviews*, 54(2), pp.49-93.
9. Zhang, Y.N., Cao, X., Larose, S. and Wanjara, P., 2012. Review of tools for friction stir welding and processing. *Canadian Metallurgical Quarterly*, 51(3), pp.250-261.
10. Song, Y., Yang, X., Cui, L., Hou, X., Shen, Z. and Xu, Y., 2014. Defect features and mechanical properties of friction stir lap welded dissimilar AA2024–AA7075 aluminum alloy sheets. *Materials & Design*, 55, pp.9-18.
11. Dubourg, L., Merati, A. and Jahazi, M., 2010. Process optimisation and mechanical properties of friction stir lap welds of 7075-T6 stringers on 2024-T3 skin. *Materials & Design*, 31(7), pp.3324-3330.

12. Soundararajan, V., Yarrapareddy, E. and Kovacevic, R., 2007. Investigation of the friction stir lap welding of aluminum alloys AA 5182 and AA 6022. *Journal of Materials Engineering and Performance*, 16(4), pp.477-484.
13. Tan, S., Zheng, F., Chen, J., Han, J., Wu, Y. and Peng, L., 2017. Effects of process parameters on microstructure and mechanical properties of friction stir lap linear welded 6061 aluminum alloy to NZ30K magnesium alloy. *Journal of Magnesium and Alloys*, 5(1), pp.56-63.
14. Movahedi, M., Kokabi, A.H., Reihani, S.S., Cheng, W.J. and Wang, C.J., 2013. Effect of annealing treatment on joint strength of aluminum/steel friction stir lap weld. *Materials & Design*, 44, pp.487-492.
15. Jana, S., Hovanski, Y. and Grant, G.J., 2010. Friction stir lap welding of magnesium alloy to steel: a preliminary investigation. *Metallurgical and Materials Transactions A*, 41(12), pp.3173-3182.
16. Akinlabi, E.T., Els-Botes, A. and McGrath, P.J., 2011, January. Effect of travel speed on joint properties of dissimilar metal friction stir welds. In *Proceedings of 2nd International Conference on Advances in Engineering and Technology (AET)*, Uganda.
17. Somasekharan, A.C. and Murr, L.E., 2004. Microstructures in friction-stir welded dissimilar magnesium alloys and magnesium alloys to 6061-T6 aluminum alloy. *Materials Characterization*, 52(1), pp.49-64.
18. Li, Y., Murr, L.E. and McClure, J.C., 1999. Solid-state flow visualization in the friction-stir welding of 2024 Al to 6061 Al. *Scripta materialia*, 40(9), pp.1041-1046.
19. Watanabe, T., Takayama, H. and Yanagisawa, A., 2006. Joining of aluminum alloy to steel by friction stir welding. *Journal of Materials Processing Technology*, 178(1-3), pp.342-349.
20. Ray, J., 2002. Delta 4 Fleet Goes from. *Medium” to “Heavy,” Spaceflight Now*, (12).
21. Kusuda, Y., 2013. Honda develops robotized FSW technology to weld steel and aluminum and applied it to a mass-production vehicle. *Industrial Robot: An International Journal*.
22. Crawford, R., Cook, G.E., Strauss, A.M., Hartman, D.A. and Stremmler, M.A., 2006. Experimental defect analysis and force prediction simulation of high weld pitch friction stir welding. *Science and Technology of Welding and Joining*, 11(6), pp.657-665.

23. Kim, Y.G., Fujii, H., Tsumura, T., Komazaki, T. and Nakata, K., 2006. Three defect types in friction stir welding of aluminum die casting alloy. *Materials Science and Engineering: A*, 415(1-2), pp.250-254.
24. Zhao, Y., Zhou, L., Wang, Q., Yan, K. and Zou, J., 2014. Defects and tensile properties of 6013 aluminum alloy T-joints by friction stir welding. *Materials & Design*, 57, pp.146-155.
25. Podržaj, P., Jerman, B. and Klobčar, D., 2015. “Welding defects at friction stir welding”. *Metalurgija*, 54(2), pp.387-389.
26. Ford, S. and Despeisse, M., 2016. Additive manufacturing and sustainability: an exploratory study of the advantages and challenges. *Journal of cleaner Production*, 137, pp.1573-1587.
27. DebRoy, T., Wei, H.L., Zuback, J.S., Mukherjee, T., Elmer, J.W., Milewski, J.O., Beese, A.M., Wilson-Heid, A.D., De, A. and Zhang, W., 2018. Additive manufacturing of metallic components—process, structure and properties. *Progress in Materials Science*, 92, pp.112-224.
28. Zhang, Y., Wu, L., Guo, X., Kane, S., Deng, Y., Jung, Y.G., Lee, J.H. and Zhang, J., 2018. Additive manufacturing of metallic materials: a review. *Journal of Materials Engineering and Performance*, 27(1), pp.1-13.
29. Gong, H., Rafi, K., Gu, H., Starr, T. and Stucker, B., 2014. Analysis of defect generation in Ti–6Al–4V parts made using powder bed fusion additive manufacturing processes. *Additive Manufacturing*, 1, pp.87-98.
30. Grasso, M. and Colosimo, B.M., 2017. Process defects and in situ monitoring methods in metal powder bed fusion: a review. *Measurement Science and Technology*, 28(4), p.044005.
31. Zhang, P., Zhou, X., Cheng, X., Sun, H., Ma, H. and Li, Y., 2020. Elucidation of bubble evolution and defect formation in directed energy deposition based on direct observation. *Additive Manufacturing*, 32, p.101026.
32. Kies, F., Wilms, M.B., Pirch, N., Pradeep, K.G., Schleifenbaum, J.H. and Haase, C., 2020. Defect formation and prevention in directed energy deposition of high-manganese steels and the effect on mechanical properties. *Materials Science and Engineering: A*, 772, p.138688.

33. Yuan, L., 2019. Solidification Defects in Additive Manufactured Materials. *JOM*, 71(9), pp.3221-3222.
34. Khodabakhshi, F., Nosko, M. and Gerlich, A.P., 2018. Effects of graphene nano-platelets (GNPs) on the microstructural characteristics and textural development of an Al-Mg alloy during friction-stir processing. *Surface and Coatings Technology*, 335, pp.288-305.
35. Hamilton, C., Dymek, S. and Sommers, A., 2008. A thermal model of friction stir welding in aluminum alloys. *International journal of machine tools and manufacture*, 48(10), pp.1120-1130.
36. Song, M. and Kovacevic, R., 2003. Thermal modeling of friction stir welding in a moving coordinate system and its validation. *International Journal of machine tools and manufacture*, 43(6), pp.605-615.
37. Schmidt, H.B. and Hattel, J.H., 2008. Thermal modelling of friction stir welding. *Scripta Materialia*, 58(5), pp.332-337.
38. Schneider, J., Beshears, R. and Nunes Jr, A.C., 2006. Interfacial sticking and slipping in the friction stir welding process. *Materials Science and Engineering: A*, 435, pp.297-304.
39. Seidel, T.U. and Reynolds, A.P., 2001. Visualization of the material flow in AA2195 friction-stir welds using a marker insert technique. *Metallurgical and materials transactions A*, 32(11), pp.2879-2884.
40. Bendzsak, G.J., North, T.H., Smith, C.B., 2000. An experimentally validated 3D model for friction stir welding, in: Proceedings of the Second International Symposium on 'Friction Stir Welding', TWI Ltd., Gothenburg, Sweden.
41. Colegrove, P.A. and Shercliff, H.R., 2005. 3-Dimensional CFD modelling of flow round a threaded friction stir welding tool profile. *Journal of materials processing technology*, 169(2), pp.320-327.
42. Dong, P., Lu, F., Hong, J.K. and Cao, Z., 2001. Coupled thermomechanical analysis of friction stir welding process using simplified models. *Science and Technology of Welding and Joining*, 6(5), pp.281-287.
43. Ulysse, P., 2002. Three-dimensional modeling of the friction stir-welding process. *International Journal of Machine Tools and Manufacture*, 42(14), pp.1549-1557.
44. Deng, X. and Xu, S., 2004. Two-dimensional finite element simulation of material flow in the friction stir welding process. *Journal of manufacturing processes*, 6(2), pp.125-133.

45. Schmidt, H. and Hattel, J., 2004. A local model for the thermomechanical conditions in friction stir welding. *Modelling and simulation in materials science and engineering*, 13(1), p.77.
46. Zhang, Z. and Zhang, H.W., 2007. Material behaviors and mechanical features in friction stir welding process. *The International Journal of Advanced Manufacturing Technology*, 35(1-2), pp.86-100.
47. Zhang, Z. and Zhang, H.W., 2008. A fully coupled thermo-mechanical model of friction stir welding. *The International Journal of Advanced Manufacturing Technology*, 37(3-4), pp.279-293.
48. Zhang, Z. and Zhang, H.W., 2009. Numerical studies on controlling of process parameters in friction stir welding. *Journal of materials processing technology*, 209(1), pp.241-270.
49. Al-Badour, F., Merah, N., Shuaib, A. and Bazoune, A., 2013. Coupled Eulerian Lagrangian finite element modeling of friction stir welding processes. *Journal of Materials Processing Technology*, 213(8), pp.1433-1439.
50. Al-Badour, F., Merah, N., Shuaib, A. and Bazoune, A., 2014. Thermo-mechanical finite element model of friction stir welding of dissimilar alloys. *The International Journal of Advanced Manufacturing Technology*, 72(5-8), pp.607-617.
51. MELD brochure, Aeroprobe corporation Available from: <http://www.aeroprobe.com/meld/> 2018.
52. Hang, Z.Y., Jones, M.E., Brady, G.W., Griffiths, R.J., Garcia, D., Rauch, H.A., Cox, C.D. and Hardwick, N., 2018. Non-beam-based metal additive manufacturing enabled by additive friction stir deposition. *Scripta Materialia*, 153, pp.122-130.
53. Rivera, O.G., Allison, P.G., Jordon, J.B., Rodriguez, O.L., Brewer, L.N., McClelland, Z., Whittington, W.R., Francis, D., Su, J., Martens, R.L. and Hardwick, N., 2017. Microstructures and mechanical behavior of Inconel 625 fabricated by solid-state additive manufacturing. *Materials Science and Engineering: A*, 694, pp.1-9.

54. Rivera, O.G., Allison, P.G., Brewer, L.N., Rodriguez, O.L., Jordon, J.B., Liu, T., Whittington, W.R., Martens, R.L., McClelland, Z., Mason, C.J.T. and Garcia, L., 2018. Influence of texture and grain refinement on the mechanical behavior of AA2219 fabricated by high shear solid state material deposition. *Materials Science and Engineering: A*, 724, pp.547-558.
55. Khodabakhshi, F. and Gerlich, A.P., 2018. Potentials and strategies of solid-state additive friction-stir manufacturing technology: A critical review. *Journal of Manufacturing Processes*, 36, pp.77-92.
56. Palanivel, S., Sidhar, H. and Mishra, R.S., 2015. Friction stir additive manufacturing: route to high structural performance. *Jom*, 67(3), pp.616-621.
57. Palanivel, S., Nelaturu, P., Glass, B. and Mishra, R.S., 2015. Friction stir additive manufacturing for high structural performance through microstructural control in an Mg based WE43 alloy. *Materials & Design (1980-2015)*, 65, pp.934-952.
58. Puleo, S.M., 2016. Additive Friction Stir Manufacturing of 7055 Aluminum Alloy.
59. Liu, G., Murr, L.E., Niou, C.S., McClure, J.C. and Vega, F.R., 1997. Microstructural aspects of the friction-stir welding of 6061-T6 aluminum. *Scripta materialia*, 37(3), pp.355-361.
60. Lee, W.B., Yeon, Y.M. and Jung, S.B., 2004. Mechanical properties related to microstructural variation of 6061 Al alloy joints by friction stir welding. *Materials transactions*, 45(5), pp.1700-1705.
61. Soundararajan, V., Zekovic, S. and Kovacevic, R., 2005. Thermo-mechanical model with adaptive boundary conditions for friction stir welding of Al 6061. *International Journal of Machine Tools and Manufacture*, 45(14), pp.1577-1587.
62. Ajri, A., Rohatgi, N. and Shin, Y.C., 2020. Analysis of defect formation mechanisms and their effects on weld strength during friction stir welding of Al 6061-T6 via experiments and finite element modeling. *The International Journal of Advanced Manufacturing Technology*, pp.1-15.
63. ASTM International. E384-17 Standard Test Method for Microindentation Hardness of Materials. West Conshohocken, PA; ASTM International, 2017. doi: <https://doi.org/10.1520/E0384-17>.

64. ASTM International. E3-11(2017) Standard Guide for Preparation of Metallographic Specimens. West Conshohocken, PA; ASTM International, 2017. doi: <https://doi.org/10.1520/E0003-11R17>.
65. ASTM International. B557-15 Standard Test Methods for Tension Testing Wrought and Cast Aluminum- and Magnesium-Alloy Products. West Conshohocken, PA; ASTM International, 2015. doi: <https://doi.org/10.1520/B0557-15>.
66. ASTM International. D1002-10(2019) Standard Test Method for Apparent Shear Strength of Single-Lap-Joint Adhesively Bonded Metal Specimens by Tension Loading (Metal-to-Metal). West Conshohocken, PA; ASTM International, 2019. doi: <https://doi.org/10.1520/D1002-10R19>
67. Kumar, K., Kalyan, C., Kailas, S.V. and Srivatsan, T.S., 2009. “An investigation of friction during friction stir welding of metallic materials”. *Materials and Manufacturing Processes*, 24(4), pp.438-445.
68. Soundararajan, V., Zekovic, S., Kovacevic, R., 2005. “Thermo-mechanical model with adaptive boundary conditions for friction stir welding of Al 6061”. *International Journal of Machine Tools and Manufacture* 45, 1577–1587.
69. Yeh, C.L., Wen, C.Y., Chen, Y.F., Yeh, S.H. and Wu, C.H., 2001. An experimental investigation of thermal contact conductance across bolted joints. *Experimental Thermal and Fluid Science*, 25(6), pp.349-357.
70. Dorbane, A., Ayoub, G., Mansoor, B., Hamade, R.F. and Imad, A., 2017. Effect of temperature on microstructure and fracture mechanisms in friction stir welded Al6061 joints. *Journal of Materials Engineering and Performance*, 26(6), pp.2542-2554.
71. Ringer, S.P. and Hono, K., 2000. Microstructural evolution and age hardening in aluminium alloys: atom probe field-ion microscopy and transmission electron microscopy studies. *Materials characterization*, 44(1-2), pp.101-131.
72. Malin, V., 1995. Study of metallurgical phenomena in the HAZ of 6061-T6 aluminum welded joints. *Welding Journal-Including Welding Research Supplement*, 74(9), p.305s.
73. Vargas, J.A., Torres, J.E., Pacheco, J.A. and Hernandez, R.J., 2013. Analysis of heat input effect on the mechanical properties of Al-6061-T6 alloy weld joints. *Materials & Design (1980-2015)*, 52, pp.556-564.

74. Esmaeili, S., Lloyd, D.J. and Poole, W.J., 2003. Modeling of precipitation hardening for the naturally aged Al-Mg-Si-Cu alloy AA6111. *Acta Materialia*, 51(12), pp.3467-3481.
75. Mrówka-Nowotnik, G. and Sieniawski, J., 2005. Influence of heat treatment on the microstructure and mechanical properties of 6005 and 6082 aluminium alloys. *Journal of Materials Processing Technology*, 162, pp.367-372.
76. Woo, W., Choo, H., Withers, P.J. and Feng, Z., 2009. Prediction of hardness minimum locations during natural aging in an aluminum alloy 6061-T6 friction stir weld. *Journal of materials science*, 44(23), pp.6302-6309.
77. Sridharan, N., Gussev, M., Seibert, R., Parish, C., Norfolk, M., Terrani, K. and Babu, S.S., 2016. Rationalization of anisotropic mechanical properties of Al-6061 fabricated using ultrasonic additive manufacturing. *Acta Materialia*, 117, pp.228-237.
78. Cakmak, E., Gussev, M.N., Sridharan, N., Seren, M.H., An, K., Wang, H. and Terrani, K.A., 2020. Micromechanical and microstructure analysis of strain-induced phenomena in ultrasonic additively-manufactured Al-6061 alloy. *Materials Science and Engineering: A*, 770, p.138533.
79. Maamoun, A.H., Xue, Y.F., Elbestawi, M.A. and Veldhuis, S.C., 2019. The effect of selective laser melting process parameters on the microstructure and mechanical properties of Al6061 and AlSi10Mg alloys. *Materials*, 12(1), p.12.
80. Uddin, S.Z., Murr, L.E., Terrazas, C.A., Morton, P., Roberson, D.A. and Wicker, R.B., 2018. Processing and characterization of crack-free aluminum 6061 using high-temperature heating in laser powder bed fusion additive manufacturing. *Additive Manufacturing*, 22, pp.405-415.
81. Jana, S., Hovanski, Y. and Grant, G.J., 2010. Friction stir lap welding of magnesium alloy to steel: a preliminary investigation. *Metallurgical and Materials Transactions A*, 41(12), pp.3173-3182.
82. Fadaeifard, F., Matori, K.A., Toozandehjani, M., Daud, A.R., Ariffin, M.K.A.M., Othman, N.K., Gharavi, F., Ramzani, A.H. and Ostovan, F., 2014. Influence of rotational speed on mechanical properties of friction stir lap welded 6061-T6 Al alloy. *Transactions of nonferrous metals society of china*, 24(4), pp.1004-1011.

83. Shirazi, H., Kheirandish, S. and Safarkhanian, M.A., 2015. Effect of process parameters on the macrostructure and defect formation in friction stir lap welding of AA5456 aluminum alloy. *Measurement*, 76, pp.62-69.
84. Naik, B.S., Chen, D.L., Cao, X. and Wanjara, P., 2013. Microstructure and fatigue properties of a friction stir lap welded magnesium alloy. *Metallurgical and Materials Transactions A*, 44(8), pp.3732-3746.
85. Dubourg, L., Merati, A. and Jahazi, M., 2010. Process optimisation and mechanical properties of friction stir lap welds of 7075-T6 stringers on 2024-T3 skin. *Materials & Design*, 31(7), pp.3324-3330.
86. Brooker, M.J., Van Deudekom, A.J.M., Kallee, S.W. and Sketchley, P.D., 2001. Applying friction stir welding to the Ariane 5 main motor thrust frame. In *Spacecraft Structures, Materials and Mechanical Testing* (Vol. 468, p. 507).
87. Baghdadi, A.H., Rajabi, A., Selamat, N.F.M., Sajuri, Z. and Omar, M.Z., 2019. Effect of post-weld heat treatment on the mechanical behavior and dislocation density of friction stir welded Al6061. *Materials Science and Engineering: A*, 754, pp.728-734.
88. Elangovan, K. and Balasubramanian, V., 2008. Influences of post-weld heat treatment on tensile properties of friction stir-welded AA6061 aluminum alloy joints. *Materials characterization*, 59(9), pp.1168-1177.